Fast beam photodissociation spectroscopy and dynamics of the vinoxy radical

David L. Osborn, Hyeon Choi, David H. Mordaunt, Ryan T. Bise, and Daniel M. Neumark
Department of Chemistry, University of California, Berkeley, California 94720, and Chemical Sciences Division, Lawrence Berkeley National Laboratory, Berkeley, California 94720

Celeste McMichael Rohlfing
Combustion Research Facility, Sandia National Laboratories, Livermore, California 94551-0969

(Received 7 October 1996; accepted 13 November 1997)

The spectroscopy and photodissociation dynamics of the vinoxy (CH_2CHO) radical $\tilde{B}(^2A'') \leftarrow \tilde{X}(^2A'')$ transition have been investigated by fast beam photofragment translational spectroscopy. We show conclusively that excitation to the $\tilde{B}$ state is followed by predissociation, even for the origin transition. Two photodissociation channels are observed: (1) CH_3+CO, and (2) $H+CH_2CO$, with a branching ratio of $\approx$1:4. The form of the translational energy distributions imply a significant exit barrier to formation of CH_3+CO, and a considerably smaller barrier for $H+CH_2CO$ formation. Dissociation ultimately proceeds by internal conversion to the ground electronic state; the internal conversion rate appears to be significantly enhanced by a curve crossing with either the $\tilde{A}(^2A')$ or $\tilde{C}(^2A')$ states. *Ab initio* calculations of critical points on the global potential energy surfaces aid in determining the dissociation mechanism. We present a simple model for dissociation over a barrier, the statistical adiabatic impulsive model, which satisfactorily reproduces the translational energy distributions. © *1997 American Institute of Physics.* [S0021-9606(97)01607-3]

I. INTRODUCTION

Molecular photodissociation is an important field of chemical physics as it offers a well-defined way of probing the forces acting between atoms and molecules in chemical reactions.[1] The dynamics of a dissociating molecule depend intimately on the shape of the potential energy surface of the system. Measurement of product state distributions can provide direct information on important features of this surface, and this prospect has motivated development of an impressive array of experimental techniques aimed at extracting such distributions.[2] While most experiments of this type have been performed on stable, closed-shell molecules, there is much to gain from the study of free radical systems using photodissociation. There are two qualitative differences between closed-shell and open-shell systems that should directly influence their photodissociation dynamics. First, the unpaired electron(s) of free radicals gives rise to more low-lying electronic states ($\leqslant$5 eV) than are typically found in stable molecules. Second, closed shell systems generally dissociate to give two radical fragments. In contrast, open-shell molecules can often dissociate to a radical and a closed-shell fragment, making this bond breaking process only mildly endothermic or even exothermic.

Experimental studies of free radical photodissociation are relatively uncommon, primarily because it is difficult to create sufficiently intense, contaminant-free sources of free radicals. To overcome this limitation, we have devised a general technique for the production of well-characterized radical samples using photodetachment of negative ion precursors. In this paper we report photodissociation spectroscopy and dynamics of the vinoxy radical, CH_2CHO. The vinoxy radical plays a key role combustion chemistry, specifically in the reactions of oxygen atoms with olefins.[3] CH_2CHO is a primary product of the reactions $O(^3P)+C_2H_4$,[4] $O(^3P)+C_2H_3$,[5] $OH+C_2H_2$,[6] and $OH+C_2H_4O$.[7] These reactions, and the CH_2CHO intermediate, are generally important since ethylene and acetylene are commonly present in combustion of larger aliphatic[8] and aromatic[9] compounds. It is therefore of considerable interest to understand the spectroscopy and dynamics of this species. This study of CH_2CHO is part of a systematic effort in our laboratory to determine how the dissociation dynamics of ''simple'' alkoxy radicals depend on the nature of the carbon bonding in the radical. The results presented here show that the dissociation dynamics of CH_2CHO, the smallest alkenoxy radical, are quite different from those of the smallest alkanoxy and alkynoxy radicals, CH_3O[10] and HCCO.[11]

The vinoxy radical has been the subject of several spectroscopic[12–19] and electronic structure[20–24] investigations. The first spectroscopic detection of CH_2CHO, discrete bands with a probable origin at 28 780 cm^{-1}, was reported by Ramsay[12] in 1965. In 1981, Hunziker[13] *et al.* reported two absorption bands of CH_2CHO: one band in the infrared originating at 8004 cm^{-1}, and a second in the ultraviolet, with its origin at 28 750 cm^{-1}. Electronic state assignments for these bands were aided by *ab initio* molecular orbital calculations by Dupuis *et al.*,[21] who predicted an ir transition, $\tilde{A}(^2A') \leftarrow \tilde{X}(^2A'')$, at 6900 cm^{-1}, and a uv transition, $\tilde{B}(^2A'') \leftarrow \tilde{X}(^2A'')$, at 26 000 cm^{-1}. The calculations predicted a planar geometry and an allylic resonance between the two valence bond structures $CH_2{=}CH{-}O\cdot$ and $\cdot CH_2{-}CH{=}O$. The latter structure was favored as the ground electronic state, with an unpaired electron primarily on the terminal carbon atom. The $\tilde{A}$ and $\tilde{B}$ states were described as primarily $CH_2{=}CH{-}O\cdot$, with the unpaired elec-

tron on the oxygen either in-plane or out-of-plane, respectively.

Lineberger and co-workers[19] established the electron affinity of CH_2CHO as 1.824 eV from negative ion photoelectron spectroscopy of CH_2CHO^-. Inoue and Akimoto[14] observed laser induced fluorescence (LIF) and dispersed fluorescence spectra of the $\tilde{B}\leftarrow\tilde{X}$ band. They assigned the vibrational modes of the radical using a triatomic model in which the three modes are the CO stretch, the CC stretch, and the CCO bend. The first experimental information on the structure of CH_2CHO was given by DiMauro, Heaven, and Miller[15] from rotationally resolved LIF spectra of the $\tilde{B}(^2A'')\leftarrow\tilde{X}(^2A'')$ transition in a supersonic jet. Based on the relative intensities of the *a*-type vs *b*-type rotational transitions (10:1) it was found that the transition dipole for the $\tilde{B}\leftarrow\tilde{X}$ transition points essentially along the CCO backbone. Their LIF spectrum refined the values of the three vibrational fundamentals in the $\tilde{B}$ state that were seen in Ref. 14 as ν_1(CO stretch)=917 cm^{-1}, ν_2(CC stretch)=1122 cm^{-1}, and ν_3(CCO bend)=450 cm^{-1}. The microwave spectra of CH_2CHO and CD_2CDO due to Endo *et al.*[16] yielded a more definitive determination of the ground state geometry that was in good agreement with the calculation of Dupuis.[21] Later *ab initio* calculations by Yamaguchi *et al.*[23] showed that the triatomic vibrational model used by Inoue and DiMauro was insufficient to describe the vibrational structure of vinoxy. Yamaguchi adopted a new numbering of the modes (which is used in this paper) based on all 12 vibrational degrees of freedom and reassigned the character of the 917 cm^{-1} fundamental as ν_8(CC stretch), and the 1122 cm^{-1} fundamental as ν_7(CH_2 rock).

Our interest in the vinoxy system was stimulated by the considerable differences between the laser-induced fluorescence and absorption spectra. The published LIF spectra[14,15] show no fluorescence above 30 200 cm^{-1} (i.e., only 1400 cm^{-1} above the $\tilde{B}$ state origin), while the absorption spectrum[13] extends to 35 700 cm^{-1}, peaking at ≈32 500 cm^{-1}. The sharply truncated LIF spectrum implies that the excited state is depleted by a fast nonradiative process. The presence of such a process is confirmed by hole-burning spectroscopy on jet-cooled vinoxy, in which Gejo *et al.*[17] measured fluorescence depletion from 30 300–33 900 cm^{-1}, finding sharp vibronic absorptions in this region where fluorescence is quenched.

Three nonradiative processes could be responsible for fluorescence quenching: direct predissociation via a repulsive state, intersystem crossing (ISC) to a quartet state, and internal conversion (IC) to the ground electronic state. The latter two processes can also lead to photodissociation. There is relatively little experimental and theoretical information on the dynamics following excitation of the $\tilde{B}$ state. Yamaguchi recently reported calculations[24] on CH_2CHO that explored the energy dependence of the $\tilde{X}$, $\tilde{A}$, $\tilde{B}$, and $\tilde{C}$ ($^2A'$) states on the C–C torsional coordinate, finding that torsional motion may couple the $\tilde{B}$ state with the $\tilde{A}$, and/or $\tilde{C}$ states. Jacox found evidence for production of CH_3+CO following uv irradiation of CH_2CHO in an Ar matrix,[25] but with a threshold near 34 500 cm^{-1}, much higher than the fluorescence cutoff energy. Previous attempts to observe photodissociation products in the gas phase using LIF have been unsuccessful.[17,18]

Our experiment directly detects the presence of photodissociation, and identifies and characterizes the photodissociation products. We can therefore readily determine if dissociation occurs following excitation of the $\tilde{B}$ state and learn about the detailed mechanism. There are several product channels which are thermodynamically feasible following uv excitation of vinoxy:

$$CH_2CHO \xrightarrow{h\nu} CH_3+CO \quad \Delta H_0^0 = 0.08\pm0.09 \text{ eV},^{26,27} \quad (1)$$

$$H+CH_2CO \qquad 1.49\pm0.09 \text{ eV}, \quad (2)$$

$$H_2+HCCO \qquad 1.56\pm0.09 \text{ eV}, \quad (3)$$

$$C_2H_2+OH \qquad 2.56\pm0.09 \text{ eV}, \quad (4)$$

$$CH_2+HCO \qquad 4.16\pm0.13 \text{ eV}. \quad (5)$$

We observe photodissociation of vinoxy to both Channels 1 and 2 over the range $28\,700 \leqslant h\nu \leqslant 33\,330$ cm^{-1} ($3.56 \leqslant h\nu \leqslant 4.13$ eV). Channels 3, 4, and 5 are not observed in this study. Our results indicate that excitation of the $\tilde{B}$ state is followed by internal conversion, eventually populating the $\tilde{X}$ state, which then dissociates via Channels 1 and 2.

The experimental apparatus and data collection methods for the present experiments are summarized in Sec. II. In Sec. III we present the photofragment yield spectrum, translational energy, and angular distribution data for CH_2CHO and CD_2CDO, in addition to *ab initio* molecular orbital calculations on this system. Section IV covers the analysis of the experimental data. Progressions in eight of the twelve vibrational modes are assigned with the aid of *ab initio* frequencies. The data analysis for Channel 2 is also presented, and we obtain the branching ratio between the two observed channels. In Sec. V, the overall dissociation mechanism is discussed. For CH_3+CO, the translational energy distributions are compared with a hybrid statistical/impulsive dissociation model. RRKM rates for the two observed channels are calculated and compared with the experimental branching ratio. Finally, the mechanism of internal conversion from the $\tilde{B}$ state is discussed. A preliminary account of these experiments has been published previously.[28]

II. EXPERIMENT

A. The fast radical beam translational spectrometer

It is generally difficult to produce a well-characterized source of free radicals using traditional molecular beam sources due to the high reactivity of open-shell species. Our experimental approach takes advantage of this instability by recognizing that most free radicals have positive electron affinities and form stable negative ion analogues. Any contaminant ions present can be separated by mass spectrometry, after which the desired neutral free radicals are generated by laser photodetachment of the corresponding

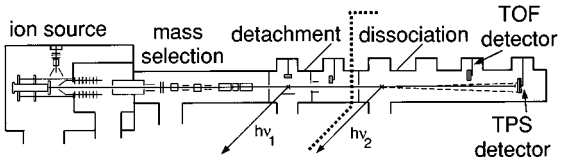

FIG. 1. The experimental apparatus. The dotted lines separate the radical production region on the left from the dissociation region on the right.

mass-selected anion. The packet of neutral radicals produced in the detachment step is then dissociated with a second laser, giving the overall scheme

$$CH_2CHO^- \overset{h\nu_1 - e^-}{\rightarrow} CH_2CHO \overset{h\nu_2}{\rightarrow} \text{fragments}. \tag{6}$$

The apparatus constructed in our laboratory, the Fast Radical Beam Photofragment Translational Spectrometer, has been described previously in detail,[29–31] and only a brief description will be given here. The apparatus is divided into two distinct regions, as shown in Fig. 1. In the first section, a clean source of free radicals is generated from a negative ion precursor. The anion precursor, CH_2CHO^-, is formed in a 60–100 Hz repetition rate pulsed supersonic expansion of 1 Torr of acetaldehyde (−78 °C) seeded in 3 atm of O_2. Acetaldehyde-d_4 is the precursor of CD_2CDO^-. A pulsed electric discharge[32] creates ions in the high pressure region before the expansion, allowing the ions to cool in the jet to rotational temperatures of typically 35–50 K. Molecular oxygen was used as a backing gas because it sustains a steady glow discharge at lower voltages than helium, neon, or argon, thereby keeping vibrational excitation of the anions to a minimum. The ions pass through a 3 mm skimmer, are accelerated to 8000 eV laboratory energy, and are mass selected using the Bakker time-of-flight method,[33] which imparts negligible energy spread to the ion beam. As the various ions separate according to their m/e ratio, a 25 ns light pulse from an excimer-pumped dye laser is fired at the appropriate time to photodetach only CH_2CHO^-. The detachment wavelength (663 nm for CH_2CHO^- and 667 nm for CD_2CDO^-) is only slightly above threshold,[19] producing radicals in their ground vibrational state. All remaining ions are deflected from the beam leaving an internally cold, high velocity beam of vinoxy radicals.

In the second section of the apparatus, after a final 1 mm collimation, the vinoxy radicals are dissociated by a frequency-doubled excimer-pumped pulsed dye laser operating between 300–350 nm, with a bandwidth of 0.3 cm^{-1}. Neutral photofragments recoiling out of the parent radical beam are detected directly, without ionization, using one of two microchannel plate (MCP) detectors. The time-of-flight (TOF) and time- and position-sensitive (TPS) detectors (described below) are located on the radical beam axis 68 and 100 cm downstream from the dissociation laser port, respectively. An aluminum strip is placed across the center of each detector to prevent undissociated parent radicals from striking the MCPs. The fragments are detected with high efficiency (typically 50%) due to their high laboratory kinetic energy. However, the MCPs are considerably less sensitive to very light fragments, such as H or D atoms, because these fragments are formed with low laboratory kinetic energies.

B. Data collection and modes of operation

Three types of experiments are performed to characterize the photodissociation of CH_2CHO. First, the energy of the photodissociation laser is scanned and the total flux of fragments is detected giving a photofragment yield (PFY) spectrum. It should be emphasized that signal is observed *only* if the radical dissociates. This experiment uses the TOF detector which can be lowered into the beam on a manipulator arm. The TOF detector has a 3 mm beam block and a simple metal anode which collects the total charge from the MCPs. The fragment signal is normalized to dissociation laser power, and also to the yield of electrons from the photodetachment of CH_2CHO^-, correcting for any variations in the radical production scheme. For vinoxy, a laser step size of 0.009 nm is used, corresponding to a step size in energy of 0.8 to 1.0 cm^{-1}. The data are calibrated at many different frequencies throughout the scanned range against the absorption spectrum of I_2,[34] with an absolute accuracy of 1 cm^{-1} or better.

In the second type of experiment, the dissociation laser is tuned to a specific photon energy of interest, and the dynamics of the dissociation process are studied. In this case, both fragments from a single parent radical are detected in coincidence using the TPS detector,[29,35] this is based on the detection scheme developed by de Bruijn and Los.[36] In this detector an 8 mm wide beam block is placed in front of a stack of three 46 mm diameter optical quality MCPs. The two electron clouds produced from the impact of the two fragments contain both spatial and temporal information describing where and when the fragments collided with the first MCP. The electron clouds are collected using a wedge and strip anode.[37,38] The spatial resolution (in the plane of the detector) is 100 μm while the relative timing resolution between the two fragment arrivals (perpendicular to the plane of the detector) is 500 ps.

From the timing and position information, we obtain the masses of the fragments, their relative translational energy E_T, and the polar angle θ between their relative velocity vector and the electric vector of the polarized dissociation laser (parallel to the ion beam axis)

$$\frac{m_1}{m_2} = \frac{r_2}{r_1}\left(1 - \frac{\nu_0 \tau}{L}\right), \tag{7}$$

$$E_T = E_0 \cdot \frac{m_1 m_2}{M} \cdot \frac{\{(\nu_0\tau)^2 + R^2\}}{L^2} \cdot \left(1 + 2\,\frac{m_1 - m_2}{M}\,\frac{\nu_0\tau}{L}\right), \tag{8}$$

$$\theta = \arctan\left(\frac{R}{\nu_0 \tau}\right). \tag{9}$$

Here, r_1 and r_2 are the distances from the center of the radical beam to each fragment on the detector face, $R = r_1 + r_2$ is the distance between the photofragments, and $\tau (= t_1 - t_2)$ is the difference in the arrival times of the fragments. M, m_1, and m_2, are the masses of the parent and

fragments respectively, ν_0 and E_0 are the laboratory velocity and energy of the parent radical, and L is the distance between the dissociation laser and the detector face. Although the relative recoil $R=r_1+r_2$ of the fragments is determined with high precision ($R/\Delta R\approx 100$) in the coincidence measurement, the individual recoils r_1 and r_2 are less precisely known, resulting in a fragment mass resolution $m/\Delta m\approx 15$.

Translational energy resolution of $\Delta E_T/E_T=0.6\%$ has been demonstrated under ideal conditions,[35] although in these experiments the resolution is somewhat coarser, typically $\Delta E_T/E_T=2.2\%$. The finite geometric acceptance of the detector is corrected by dividing the raw data by a detector acceptance function,[29] which gives the probability of observing a coincidence even at each combination of E_T and θ.

Due to the geometry of the detector, the coincidence detection scheme is only practical when the mass ratio of the fragments $m_1/m_2\leqslant 5$. For mass ratios larger than 5, there is very little probability of detecting both particles in coincidence; if the heavy fragment has enough energy to clear the beam block in front of the MCPs, the light fragment recoils past the edge of the detector. Channels 2 and 3 fall into this category where the mass disparity is too large for the coincidence experiment.

In order to detect Channels 2 and 3, a third type of experiment is performed that is sensitive to product channels even if $m_1/m_2>5$. This is a less detailed, noncoincidence experiment[31] in which the flight time of the fragments from the dissociation laser to the TOF detector is recorded using a transient digitizer with 1 ns bin width. The narrow beam block, (3 mm) on this detector allows improved collection of heavy fragments compared to the TPS detector described above. The resulting TOF distributions are a one-dimensional projection of the photofragment velocity distribution in the laboratory frame along the beam axis. These results are more averaged than the $P(E_T,\theta)$ distributions obtained with the TPS detector, but in return are sensitive to all product channels because two-particle coincidence detection is not required. This method is particularly useful for detecting light atom fragments such as H or D atoms, because these will have a much larger spread in arrival times at the detector and should thus be readily distinguishable from the heavier fragments. Pairs of TOF distributions are acquired at each photon energy with the dissociation laser polarized either parallel or perpendicular to the radical beam axis. The analysis of these data is discussed in Sec. IV.

III. RESULTS

Our results from the three types of experiments are given in this section, followed by a description of the electronic structure calculations on the vinoxy system. Before presenting spectra of the vinoxy radical, we point out that the anion we photodetach at m/e 43 is in fact CH_2CHO^-, and not the isomer CH_3CO^-. While the two species are indistinguishable in the parent ion mass spectrum, they have very different photodetachment spectra. CH_2CHO^-, the more stable ion of the two, has an electron affinity (EA) of 1.824 eV,[19] while CH_3CO^- has an EA of 0.423 eV.[39] The photoelectron spectrum of m/e 43 ions measured on a different apparatus in our laboratory (using the identical ion source as in the photodissociation study) is in quantitative agreement with the literature spectrum of CH_2CHO^-.[19] Therefore, we are confident that all photodissociation spectra reported here arise unambiguously from the CH_2CHO radical. Our photoelectron spectrum shows a small amount of vibrationally excited radicals produced from photodetachment of vibrationally excited anions, but their concentration is too low to substantially affect the results presented here.

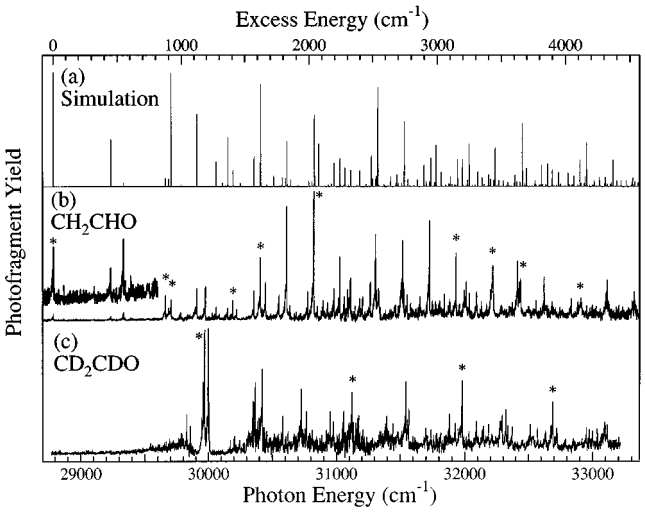

FIG. 2. Photofragment yield spectra of the vinoxy radical. Energy in excess of the $\tilde{B}\leftarrow\tilde{X}$ 0_0^0 transition is given along the top abscissa. (a) Simulation of CH_2CHO, (b) CH_2CHO experimental data, (c) CD_2CDO experimental data. Translational energy and angular distributions in Figs. 4 and 5 were acquired at the vibronic transitions marked with *.

A. Photofragment yield spectra

The PFY spectra obtained from excitation of the $\tilde{B}(^2A'')\leftarrow\tilde{X}(^2A'')$ transition are shown in Figs. 2(b) and 2(c) for CH_2CHO and CD_2CDO, respectively. The spectra show extended vibrational progressions in the excited electronic state with narrow linewidths, indicative of fragmentation by predissociation rather than by direct excitation to a repulsive potential energy surface. Peak positions and intensities for CH_2CHO and CD_2CDO are given in Tables I and II. Our transition energies agree quantitatively with those of DiMauro *et al.*,[15] but disagree with the measurements of Inoue and Akimoto[14] by as much as 45 cm^{-1}.

The published LIF spectra[14,15] of CH_2CHO show features up to 1400 cm^{-1} above the 0_0^0 transition. All these fluorescent levels are observed in our PFY spectra, indicating a competition between fluorescence and predissociation. The origin transition is the strongest line in the LIF spectrum,[15] but very weak in the PFY spectrum, indicating that the quantum yield for dissociation (Φ_{diss}) of 0_0^0 is small. Nonetheless, measurable dissociation occurs across the entire band, including the origin. The intensities in the PFY spectrum rapidly increase as the photon energy is raised, even though the Franck–Condon factors for absorption increase only slightly, indicating a steep rise in Φ_{diss}. Above 1400 cm^{-1} of excess

TABLE I. Peak positions (cm^{-1}), intensities, and vibrational assignments for the PFY spectrum of CH_2CHO, Fig. 2(b).

ν	$\nu-\nu_0$	I	Assignment	ν	$\nu-\nu_0$	I	Assignment	ν	$\nu-\nu_0$	I	Assignment
28 785.6	0.0	55	0_0^0	30 822.3	2036.7	1000	$7_0^1\ 8_0^1$	31 931.0	3145.4	523	$7_0^2\ 8_0^1$
29 234.6	449.0	34	9_0^1	30 850.2	2064.6	112	$4_0^1\ 9_0^1$	31 957.3	3171.7	131	
29 333.3	547.7	66	11_0^2	30 893.4	2107.8	156		31 995.1	3209.5	235	
29 659.1	873.5	195	10_0^2	30 926.9	2141.3	140	$6_0^1\ 10_0^2$	32 002.8	3217.2	184	
29 684.1	898.5	99	9_0^2	30 976.7	2191.1	250	$6_0^1\ 8_0^1$	32 011.6	3226.0	302	
29 703.2	917.6	166	8_0^1	31 024.3	2238.7	496	7_0^2	32 032.0	3246.4	213	
29 781.0	995.4	65	$9_0^1\ 11_0^2$	31 058.9	2273.3	187	$8_0^2\ 9_0^1$	32 091.4	3305.8	227	
29 908.2	1122.6	251	7_0^1	31 084.5	2298.9	242		32 127.6	3342.0	150	
29 976.0	1190.4	265	$8_0^1\ 11_0^1$?	31 104.6	2319.0	311		32 167.6	3382.0	130	
30 030.7	1245.1	62		31 111.0	2325.4	331		32 200.1	3414.5	240	
30 059.8	1274.2	107	6_0^1	31 144.8	2359.2	117		32 217.8	3432.2	428	
30 085.4	1299.8	52		31 181.5	2395.9	170		32 413.2	3627.6	461	
30 150.3	1364.7	97	$8_0^1\ 9_0^1$	31 205.3	2419.7	186		32 426.2	3640.6	301	
30 192.5	1406.9	158	5_0^1	31 266.1	2480.5	296		32 435.2	3649.6	323	
30 221.8	1436.2	90		31 307.7	2522.1	665	$4_0^1\ 8_0^1$	32 557.3	3771.7	157	
30 355.1	1569.5	233	$7_0^1\ 9_0^1$	31 331.8	2546.2	248		32 622.0	3836.4	338	
30 407.4	1621.8	491	4_0^1	31 519.4	2733.8	620	$4_0^1\ 7_0^1$	32 832.1	4046.5	173	
30 448.4	1662.8	298	$7_0^1\ 11_0^2$	31 527.9	2742.3	295		32 907.9	4122.3	169	
30 546.0	1760.4	135		31 553.2	2767.6	202		33 111.1	4325.5	315	
30 553.0	1767.4	201		31 653.2	2867.6	165		33 318.0	4532.4	228	
30 612.3	1826.7	885	8_0^2	31 725.2	2939.6	772	$7_0^1\ 8_0^2$				
30 633.6	1848.0	118	$5_0^1\ 9_0^1$	31 840.8	3055.2	205					
30 773.9	1988.3	224	$7_0^1\ 10_0^2$	31 883.0	3097.4	166					

energy, where the LIF signal is strongly quenched, we expect that $\Phi_{diss} \cong 1$, and our overall intensities are in accord with low-resolution absorption[13] and high resolution hole-burning[17] data. Each vibrational transition in Fig. 2 is in fact composed of many rovibronic transitions. The sharp spike that dominates each vibrational transition represents a bandhead in the R branch of the rotational contour, as first analyzed by DiMauro *et al.*[15] However, due to the higher rotational temperature in our supersonic expansion ($\approx$30–50 K) and limited laser resolution, it is not possible to discern whether lifetime broadening occurs in the PFY spectra above 1400 cm^{-1}.

For CD_2CDO no LIF spectrum has been published, although a spectrum was acquired by Inoue and Akimoto,[14] who reported only the positions of three peaks at 28 840, 29 608, and 29 820 cm^{-1}. The values for excess energy in the $\tilde{B}$ state given in Table II are calculated under the assumption that the first peak observed by Inoue is the 0_0^0 transition of CD_2CDO. In the PFY spectrum of CD_2CDO in Fig. 2(c), the lowest transitions show no detectable signs of predissociation, and the shape of the overall spectrum, punctuated by the strong feature near 30 000 cm^{-1}, is quite different from the CH_2CHO data. A gradual increase in the intensity of unstructured signal with photon energy is present in the spectra of both isotopes, but is much more pronounced for CD_2CDO. The unstructured component is not present in background scans taken with the photodissociation laser blocked, demonstrating that this broad signal is due to photofragments of the parent radical.

TABLE II. Peak positions (cm^{-1}) and intensities for the PFY spectrum of CD_2CDO, Fig. 2(c).

ν	$\nu-\nu_0{}^a$	I	ν	$\nu-\nu_0$	I	ν	$\nu-\nu_0$	I
29 828.4	988.4	320	30 583.1	1743.1	310	32 092.4	3252.4	264
29 858.0	1018.0	230	30 726.6	1886.6	523	32 144.2	3304.2	228
29 945.1	1105.1	293	30 767.7	1927.7	343	32 185.4	3345.4	244
29 957.8	1117.8	575	30 949.6	2109.6	344	32 294.2	3454.2	315
29 970.6	1130.6	987	30 975.0	2135.0	264	32 323.9	3483.9	361
29 977.4	1137.4	216	31 056.2	2216.2	344	32 337.8	3497.8	234
29 997.4	1157.4	1000	31 122.0	2282.0	496	32 371.5	3531.5	224
30 006.8	1166.8	416	31 397.0	2557.0	305	32 504.1	3664.1	245
30 173.5	1333.5	116	31 546.8	2706.8	578	32 573.0	3733.0	209
30 200.2	1360.2	130	31 559.0	2719.0	284	32 635.2	3795.2	190
30 207.1	1367.1	148	31 568.4	2728.4	363	32 689.8	3849.8	422
30 247.7	1407.7	118	31 882.5	3042.5	326	32 719.2	3879.2	212
30 369.7	1529.7	569	31 927.6	3087.6	250	33 096.3	4256.3	260
30 423.0	1583.0	679	31 979.6	3139.6	588	33 111.9	4271.9	239

[a]Energy in excess of the 0_0^0 transition measured by Inoue and Akimoto at 28 840 cm^{-1}.

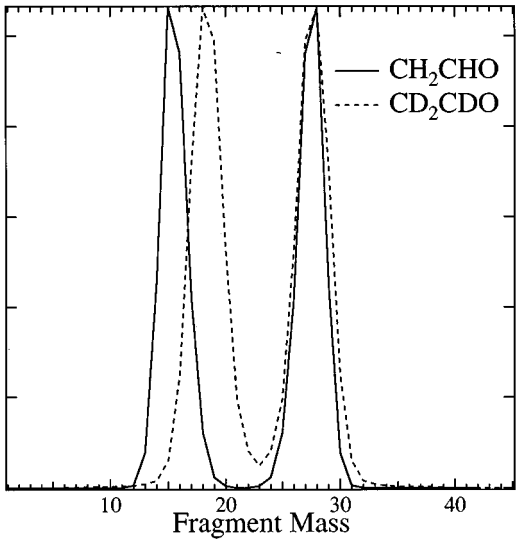

FIG. 3. Photofragment mass spectrum of CH_2CHO and CD_2CDO. Note that the higher mass peak ($m=28$) does not shift upon deuteration and must be assigned to CO. The cofragments are CH_3 and CD_3, respectively.

B. Coincidence photofragment distributions: CH_3+CO

Using the TPS detector, we perform coincidence measurements to probe for dissociation via Channels 1, 4, and 5. For this set of experiments, the photodissociation laser is fixed on one of the peaks marked in Fig. 2 and both fragments are detected in coincidence. The photofragment mass spectrum is easily found by conservation of linear momentum in the center of mass frame according to Eq. (7), and is presented in Fig. 3 for both CH_2CHO and CD_2CDO. Despite the limited fragment mass resolution of $m/\Delta m \approx 15$, the use of both isotopes of vinoxy demonstrates that the heavy fragment contains no hydrogen atoms. Therefore, the only product channel observed *in coincidence* is Channel 1, CH_3+CO. We see no evidence for production of C_2H_2+OH or CH_2+HCO. The results for Channel 2, $H+CH_2CO$, will be discussed in Sec. III C.

Once the identity of the fragments are known, the coupled translational energy and angular distribution, $P(E_T,\theta)$, is determined by direct inversion of the data using Eqs. (8) and (9) along with the calculated detector acceptance function.[29] The two dimensional $P(E_T,\theta)$ distribution can be separated into an angle-independent translational energy distribution $P(E_T)$, and an energy-dependent anisotropy parameter,[20] that describes the angular distribution of the fragments

$$P(E_T,\theta)=P(E_T)\cdot\{1+\beta(E_T)P_2(\cos\,\theta)\}. \tag{10}$$

The limiting cases of $\sin^2\theta$ and $\cos^2\theta$ angular distributions are given by $\beta=-1$ and $+2$, respectively. Together, the $P(E_T)$ and $\beta(E_T)$ distributions can yield detailed information on the dynamics of the dissociation process.

In analyzing the current experiment, E_T is binned in 30 meV increments, while θ is binned in 1° increments. The general data analysis scheme remains the same as in previous papers, with the exception of one refinement in the analysis

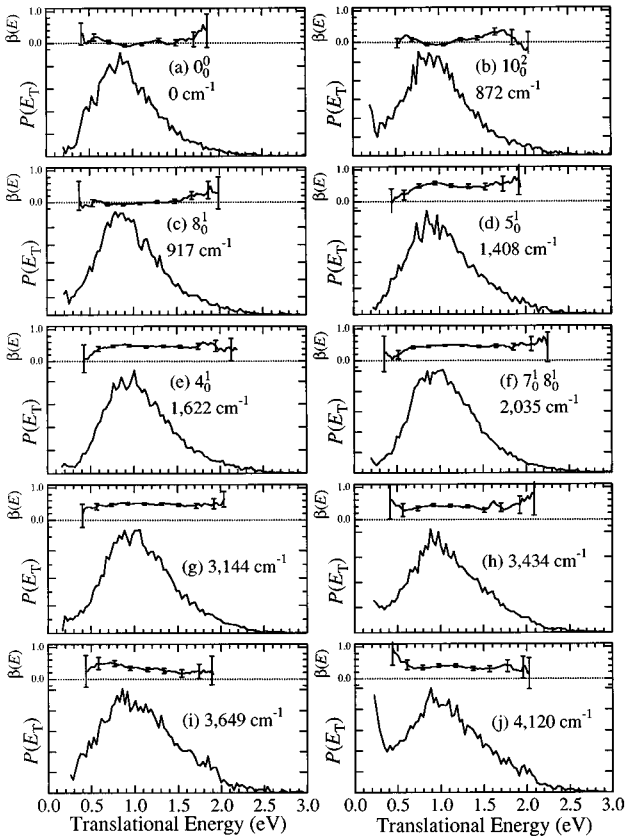

FIG. 4. Photofragment translational energy distributions $P(E_T)$ and angular distributions $\beta(E_T)$ for CH_3+CO. Statistical error bars on $\beta(E_T)$ represent $\pm 1\sigma$. Vibronic assignments are given in addition to the excess energy for each transition when possible.

of the angular distributions that yields more smoothly varying functions of the anisotropy parameter β with E_T. The data are divided into translational energy windows of width 0.4 eV, where E' is a running parameter such that $E' \leqslant E_T \leqslant (E'+0.4\text{ eV})$. β is assumed to be constant over this 0.4 eV window and is determined from a linear least squares fit of the distribution $P(E_T,\theta)$ to Eq. (10) with $P(E_T)$ and β as the fitting parameters. The quantity E' is then incremented in 30 meV steps beginning with $E'=0$ and the fitting procedure is repeated until the entire energy range of the data is covered. In other words, $\beta(E_T)$ is constructed as a moving average over 0.4 eV windows in E_T. Using these values of $\beta(E_T)$, a second linear least squares fit in the single parameter $P(E_T)$ is determined for each individual 30 meV wide energy bin, completing the separation of $P(E_T,\theta)$ into two one dimensional distributions, i.e., $P(E_T)$ and $\beta(E_T)$.

The resulting $P(E_T)$ and $\beta(E_T)$ distributions for photodissociation of vinoxy yielding CH_3+CO and CD_3+CO are shown in Figs. 4 and 5, respectively, for the vibrational levels noted in Fig. 2. Each data set consists of 10 000 to 40 000 coincident events. The translational energy distributions are similar at all photon energies for both isomers, peaking at $\approx$0.9 eV. Both the width of the distributions and the most probable translational energy increase slightly as the photon

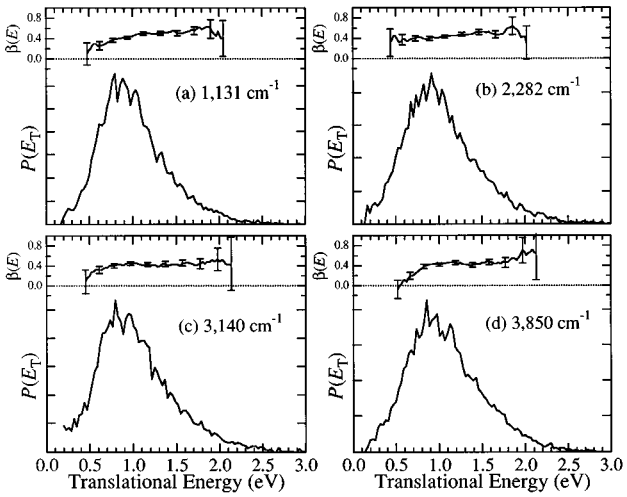

FIG. 5. Photofragment translational energy distributions $P(E_T)$ and angular distributions $\beta(E_T)$ for CD_3+CO. Statistical error bars on $\beta(E_T)$ represent $\pm 1\sigma$. Excess energy above the origin is referenced to Inoue and Akimoto's value (Ref. 14) for $0_0^0 = 28\,840\ cm^{-1}$.

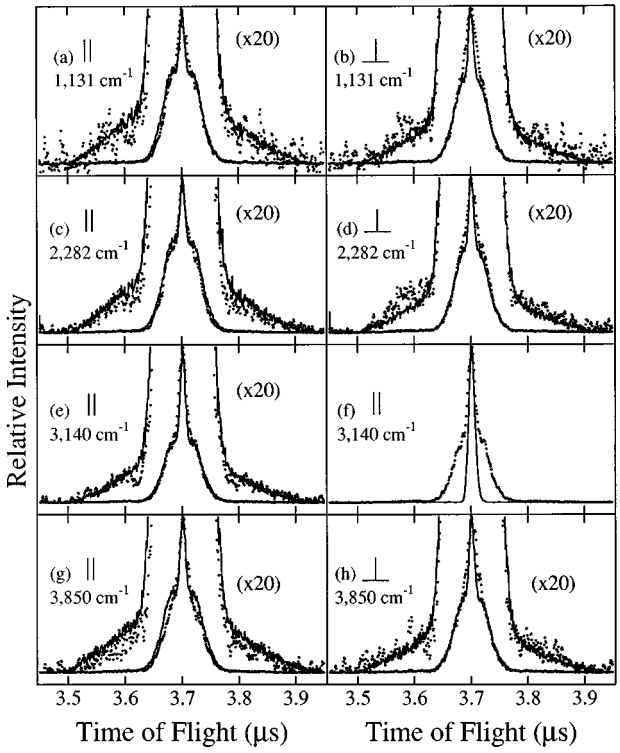

FIG. 6. Photofragment time-of-flight distributions for all photon energies used in Fig. 5. Laser polarization is either parallel (∥) or perpendicular (⊥) to the radical beam axis. Circles are the experimental data. For all panels except (f), the solid lines give total simulation. In panel (f), the solid line is the experimental TOF distribution of parent radicals (CD_2CDO) taken with the detector displaced 10 mm vertically.

energy is increased, but the changes are minor. The angular distributions are isotropic ($\beta \cong 0$) at the lowest three photon energies. However, anisotropic distributions with $\beta(E_T) > 0$ are observed at all energies 1408 cm^{-1} and higher above the $\tilde{B}$ state origin. This apparently abrupt change coincides with the large drop in fluorescence quantum yield, and indicates that the dissociation rate increases markedly between 917 and 1408 cm^{-1} excess energy.

C. Noncoincidence photofragment distributions

To determine whether the $\tilde{B}$ state of vinoxy also decays through Channels (2) and (3), noncoincident TOF distributions for CD_2CDO dissociation are obtained using the third type of experimental configuration described in Sec. II B. The data are shown as circles in Fig. 6, and Fig. 7 shows one of these spectra in greater detail. The four photon energies chosen correspond to the four coincidence spectra in Fig. 5. TOF distributions are presented only for CD_2CDO, because the detection efficiency of the MCPs for D atoms is substantially greater than for H atoms due to the higher laboratory kinetic energy of the heavier isotope. Even for D atoms, the detection efficiency appears to be ≈8% (see Sec. IV B) of that for heavy fragments such as CD_3 or CO.

The appearance of all the TOF spectra is roughly the same. Each consists of a sharp spike superimposed on a broader peak that is about 100 ns wide. There is also a very broad, weak feature from 3.5 to 3.9 μs, better seen at 20× magnification, which has a FWHM of ≈10 times that of the sharp spike. The sharp spike is only slightly broader than the TOF distribution of the undissociated parent radicals [measured by moving the TOF detector off-center by several mm; see Fig. 6(f)], implying that these fragments have very little velocity imparted to them by the dissociation process. The broad, weak feature arises from fragments which are significantly forward/backward scattered by the dissociation event. It is therefore a reasonable conclusion that these two features represent the heavy and light fragments, respectively, of a dissociation channel whose mass ratio is at least 10:1. The

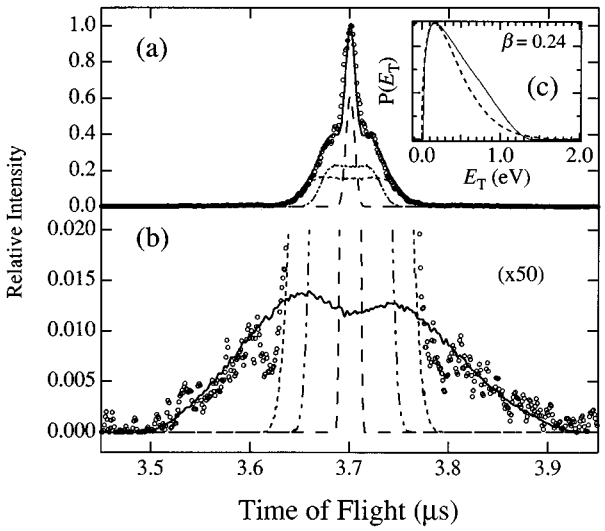

FIG. 7. CD_2CDO TOF distribution for 3140 cm^{-1} excess energy, showing individual fragment contributions. Experimental data (○), CD_2CO (– –), CO (– – – –), CD_3 (---). (a) sum of all contributions (—); (b) Magnification to show D atom contribution (—); (c) $P(E_T)$ distribution (—) for this fit, with prior distribution also shown for comparison (---).

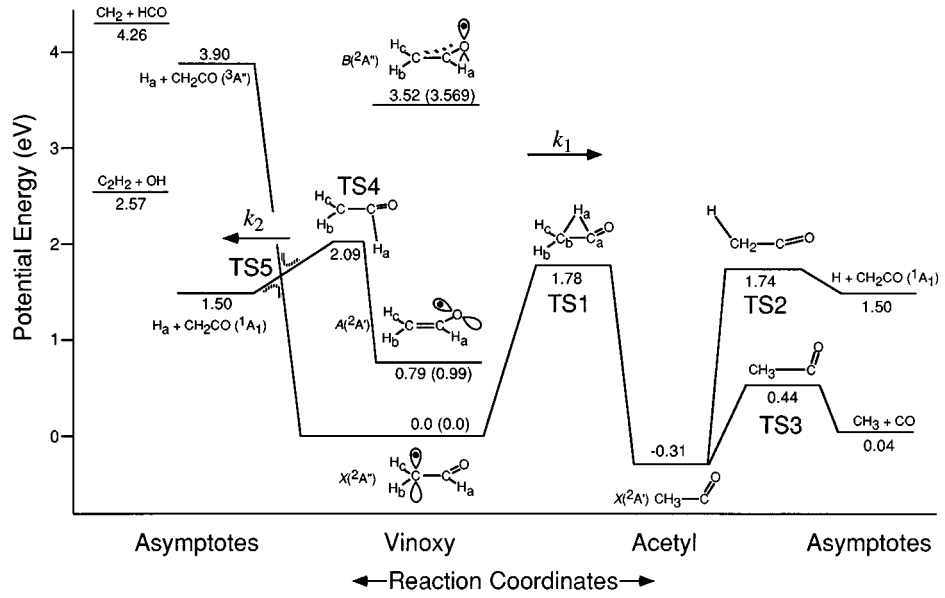

FIG. 8. Schematic of potential energy surfaces of the vinoxy radical system. All energies are in eV, include zero-point energy, and are relative to CH_2CHO $\tilde{X}(^2A'')$. Calculated energies are compared, when possible, with experimentally determined values in parentheses. Transition states 1–5 are labeled, along with the rate constant definitions from RRKM calculations. The solid potential curves to the left of vinoxy retain C_s symmetry. The avoided crossing (dotted lines) which forms TS5 arises when C_s symmetry is broken by out-of-plane motion.

analysis in Sec. IV B shows that these two features are from the $D+CD_2CO$ channel, and that the 100 ns wide peak under the spike is from the CD_3+CO channel.

D. *Ab initio* electronic structure calculations

To supplement the experimental data and aid in interpreting our results, we have performed *ab initio* molecular orbital calculations using the GAUSSIAN 92[41] and GAUSSIAN 94[42] suite of programs. Our main goal is to characterize stationary points on both ground and excited state potential energy surfaces. The calculated energies, structures, and vibrational frequencies at various minima and transition states are very useful in assigning the PFY spectra in Fig. 2 and understanding the photodissociation dynamics of the system. The absolute and relative energetics of the various minima, transition states, and asymptotic states relevant to the vinoxy system are shown in Fig. 8 and tabulated in Table III, while geometries and vibrational frequencies are listed in Tables IV and V. Figure 8 is a schematic representation of the surfaces involved in this system, sections of which have been previously investigated by Donaldson *et al.*[5] and Deshmukh *et al.*[43] The zero of energy is chosen to be the zero-point level of the CH_2CHO $\tilde{X}(^2A'')$ potential well. The only experimentally determined barrier height is that for dissociation of acetyl (CH_3CO) to CH_3+CO, (TS3), found to be 0.75 ± 0.02 eV.[44,45] This agrees well with our calculated barrier height $0.44+0.31=0.75$ eV, with respect to the CH_3CO well.

We have used the G2[46] and G2Q[47] methodologies for the ground state surface. These methods have been compared extensively with experimental thermodynamic values and give accurate (± 0.1 eV) estimations of dissociation energies. Because the single determinant wave functions in the G2 treatment do not work well for excited states, we have also performed multiconfigurational complete active space self consistent field (CASSCF) calculations[48] for the $\tilde{X}$, $\tilde{A}$, and $\tilde{B}$ electronic states of vinoxy with the 6-31G** basis set. Building on earlier work,[21,23,24] we choose an active space which consists of three electrons in the three a'' orbitals [CAS(3,3)] for the $\tilde{X}$ and $\tilde{B}$ states, while for the $\tilde{A}$ state the a'' lone pair on oxygen is excluded and the singly occupied a' orbital on oxygen is included in the active space. The agreement with earlier calculations[21,23,24] is very good with respect to energies, geometries, and frequencies. We refine the CASSCF

TABLE III. *Ab initio* energies of stationary points in Fig. 8.

Method	Species	Relative energy[a]
G2/G2Q	CH_2CHO $\tilde{X}(^2A'')$	0.0
	CH_3CO $\tilde{X}(^2A')$	−0.31
	TS1	1.78
	TS2	1.74
	TS3	0.44
	CH_3+CO	0.04
	$H+CH_2CO$ $\tilde{X}(^1A_1)$	1.50
	$H+CH_2CO$ $\tilde{a}(^3A'')$	3.90
	C_2H_2+OH	2.57
	CH_2+HCO	4.26
CASSCF(3,3)-MP2/6-31G**	CH_2CHO $\tilde{X}(^2A'')$	0.0
	CH_2CHO $\tilde{A}(^2A')$	0.73
	CH_2CHO $\tilde{B}(^2A'')$	3.52
CASSCF(5,5)-MP2/6-31G**	CH_2CHO $\tilde{X}(^2A'')$	0.0
	CH_2CHO $\tilde{A}(^2A')$	0.79
	TS4	2.09
Experiment	CH_2CHO $\tilde{A}(^2A')$	0.99[b]
	CH_2CHO $\tilde{B}(^2A'')$	3.569[c]

[a]Total energy relative to the zero-point level of CH_2CHO, in eV.
[b]Reference 13.
[c]Reference 15.

TABLE IV. *Ab initio* geometries and frequencies of stationary points in Fig. 8.[a]

$CH_2CHO\ \tilde{X}(2A'')$[b,c]	$CH_2CHO\ \tilde{A}(2A')$[d]	CH_3CO[b,c]	TS1[e]	TS2[e]	TS3[e]	TS4[d]	TS5[f]
			Geometries				
$r(C_aC_b)=1.456$	$r(C_aC_b)=1.333$	$r(C_aC_b)=1.513$	$r(C_aC_b)=1.410$	$r(C_aC_b)=1.340$	$r(C_aC_b)=2.113$	$r(C_aC_b)=1.324$	
$r(C_aO)=1.200$	$r(C_aO)=1.348$	$r(C_aO)=1.196$	$r(C_aO)=1.204$	$r(C_aO)=1.163$	$r(C_aO)=1.147$	$r(C_aO)=1.195$	
$r(C_bH_c)=1.082$	$r(C_bH_c)=1.074$	$r(C_bH_c)=1.092$	$r(C_bH_c)=1.094$	$r(C_bH_c)=1.083$	$r(C_bH_c)=1.087$	$r(C_bH_c)=1.068$	
$r(C_bH_b)=1.082$	$r(C_bH_b)=1.072$	$r(C_bH_b)=1.092$	$r(C_bH_b)=1.083$	$r(C_bH_b)=1.083$	$r(C_bH_b)=1.087$	$r(C_bH_b)=1.073$	
$r(C_aH_a)=1.110$	$r(C_aH_a)=1.098$	$r(C_bH_a)=1.093$	$r(C_bH_a)=1.481$	$r(C_bH_a)=1.888$	$r(C_bH_a)=1.085$	$r(C_aH_a)=1.66$	
$\angle(C_bC_aO)=123.6$	$\angle(C_bC_aO)=124.7$	$\angle(C_bC_aO)=127.5$	$\angle(C_bC_aO)=139.3$	$\angle(C_bC_aO)=172.1$	$\angle(C_bC_aO)=115.1$	$\angle(C_bC_aO)=157.5$	
$\angle(H_cC_bC_a)=118.7$	$\angle(H_cC_bC_a)=121.8$	$\angle(H_cC_bC_a)=108.6$	$\angle(H_cC_bC_a)=122.0$	$\angle(H_cC_bC_a)=116.7$	$\angle(H_cC_bC_a)=99.6$	$\angle(H_cC_bC_a)=121.2$	
$\angle(H_bC_bC_a)=121.3$	$\angle(H_bC_bC_a)=119.6$	$\angle(H_bC_bC_a)=108.6$	$\angle(H_bC_bC_a)=117.8$	$\angle(H_bC_bC_a)=116.7$	$\angle(H_bC_bC_a)=99.6$	$\angle(H_bC_bC_a)=118.3$	
$\angle(H_aC_aO)=121.5$	$\angle(H_aC_aO)=111.4$	$\angle(H_aC_bC_a)=111.1$	$\angle(H_aC_bC_a)=52.6$	$\angle(H_aC_bC_a)=111.3$	$\angle(H_aC_bC_a)=103.1$	$\angle(H_aC_aO)=98.5$	
		$\angle(H_cC_bC_aO)=121.6$	$\angle(H_cC_bC_aO)=117.0$	$\angle(H_cC_bC_aO)=105.0$	$\angle(H_cC_bC_aO)=59.5$		
		$\angle(H_bC_bC_aO)=-121.6$	$\angle(H_bC_bC_aO)=-68.5$	$\angle(H_bC_bC_aO)=-105.0$	$\angle(H_bC_bC_aO)=-59.5$		
		$\angle(H_aC_bC_aO)=0.0$[g]	$\angle(H_aC_bC_aO)=0.0$	$\angle(H_aC_bC_aO)=0.0$[g]	$\angle(H_aC_bC_aO)=180.0$[g]		
			Frequencies				
3081	3431	2950	3276 (V)[h]	3304	3276	3465	3100
2985	3336	2946	3098 (V)	3202	3260	3349	3100
2901	3107	2871	1966 (V)	2194	3105	2026	1700
1441	1773	1913	1846 (V)	1425	2044	1584	1450
1392	1550	1433	1465 (V)	1118	1453	1190	1300
1267	1352	1432	1229 (T)	1033	1446	1100	1200
1089	1183	1356	1126 (T)	799	939	714	1150
947	1025	1037	1036 (V)	571	611	592	700
910	956	938	836 (R)	567	547	542	700
704	864	827	633 (V)	426	277	432	700
482	714	454	438 (R)	309	43	169	400
474	484	85	1675*i* (T)	801*t*	466*t*	1504*t*	

[a]See Fig. 8 for atom label definitions.
[b]Geometry from G2 method: MP2/6-31G*.
[c]Frequencies from G2 method: UHF/6-31G* scaled by 0.8929.
[d]Geometry and frequencies are CASSCF(5,5)/6-31G**.
[e]Geometry and frequencies from G2Q method: QCISD/6-311G**.
[f]Frequencies estimated from Ref. 65.
[g]Fixed.
[h]Motion into which vibrations develop asymptotically. See Sec. V B 2.

energetics using single point CASSCF-MP2[49] to include dynamic electron correlation.

The direct bond cleavage $CH_2CHO \rightarrow H(^2S)+CH_2CO$ requires a CASSCF wave function to properly describe the spin coupling, since the ground state of vinoxy in C_s symmetry correlates with $CH_2CO\ \tilde{a}\ (^3A'')$, while the $\tilde{A}$ state of vinoxy correlates with $CH_2CO\ \tilde{X}(^1A_1)$. For dissociation along the reaction coordinate leading to triplet ketene, five electrons are distributed among five orbitals [CAS(5,5)], which are chosen to be the C–H_a σ bond ($10a'$), the C–O π bond ($1a''$), the unpaired electron on the methylene C ($2a''$), the C–O π^* orbital ($3a''$), and the C–H_a σ^* orbital ($11a'$). This active space contains the most important configurations needed to describe the breaking of the C–H_a bond along with the resonance character of the CCO backbone as described by Dupuis *et al.*[21] The C–H_a cleavage of $CH_2CHO\ \tilde{A}(^2A')$ to singlet ketene is investigated by a similar extension of the active space. Again, the energetics are refined using CASSCF-MP2.

A comparison of calculated and experimental excited state energies in Table III shows that the CASSCF-MP2 treatment gives a fairly good description of the vinoxy energetics. However, Table V shows that the CASSCF vibrational frequencies are systematically too high compared to experiment, and that the calculated C–C and C–O bond lengths for the $\tilde{X}(^2A'')$ state differ considerably from the experimental values. A CASSCF calculation of the geometry by Yamaguchi[24] using a larger (DZP) basis set yields results similar to ours, indicating that the good agreement found by Dupuis[21] between the experimental and *ab initio* geometry of the $\tilde{X}(^2A'')$ state (using a smaller 3-21G basis) was probably fortuitous. The disagreement arises mainly because CASSCF neglects dynamic electron correlation. To obtain a benchmark for the CASSCF error in the excited state geometries and frequencies, we have performed a QCISD[50]/6-31G** geometry optimization and frequency calculation on $CH_2CHO\ \tilde{X}(^2A'')$. From this comparison we have an estimate of the error in the calculated CASSCF vibrational frequencies for the $\tilde{B}$ state, which cannot be calculated using QCISD.

The results given in Table V demonstrate that the bond lengths are in better agreement with the microwave values than previous multiconfigurational studies. The agreement is not yet quantitative, as the QCISD C–C bond length is 0.026 Å longer and C–O bond length 0.020 Å shorter than experiment, respectively. Compared to the CASSCF frequencies, the QCISD frequencies are consistently lower for the 9 a' modes and roughly equal for the 3 a'' modes, and are therefore in improved agreement with experimental values from

TABLE V. Comparison of CASSCF/6-31G**, QCISD/6-31G**, and experimental geometries and frequencies.[a]

Method	$\tilde{X}(^2A'')$ CAS(3,3)	$\tilde{X}(^2A'')$ QCISD	Experiment	$\tilde{B}(^2A'')$ CAS(3,3)	Experiment
$r(C_aC_b)$[b]	1.436	1.434	1.408[c]	1.450	1.466[d,e]
$r(C_aO)$	1.224	1.241	1.261[c]	1.360	1.337
$r(C_bH_c)$	1.073	1.080	1.081[e]	1.072	1.069[e]
$r(C_bH_b)$	1.073	1.081	1.080[g]	1.071	1.069[e]
$r(C_aH_a)$	1.089	1.100	1.088[g]	1.075	1.069[e]
$\angle(C_bC_aO)$	122.6	122.6	122.4[c]	121.5	129.5
$\angle(H_cC_bC_a)$	119.4	119.2		120.1	
$\angle(H_bC_bC_a)$	121.0	121.2		119.9	
$\angle(H_aC_aO)$	119.7	120.4		116.8	
$\nu_1(C_bH_cH_b$ asym. str.) a'	3447	3353		3460	
$\nu_2(C_bH_cH_b$ sym. str.) a'	3333	3233		3348	
$\nu_3(C_aH_a$ stretch) a'	3207	3057		3362	
$\nu_4(C_aO$ stretch) a'	1666	1593	1540[f]	1881	1623[g]
$\nu_5(C_bH_cH_b$ scissors) a'	1598	1522	1454	1561	1407
$\nu_6(OC_aH_a$ bend) a'	1519	1439	1361	1438	1274
$\nu_7(C_bH_cH_b$ rock) a'	1216	1179	1141	1212	1123
$\nu_8(C_aC_b$ stretch) a'	1036	993	949	998	918
$\nu_9(C_bC_aO$ bend) a'	537	507	498	480	449
$\nu_{10}(C_aH_a$ wag) a''	981	977		453	437
$\nu_{11}(C_aC_b$ torsion) a''	467	446		245	274
$\nu_{12}(C_bH_cH_b$ wag) a''	666	713		267	

[a]Polarization functions on H with CAS(3,3) accomplish a similar lowering of the a'' vibrational frequencies found from a larger CAS in Ref. 24.
[b]See Fig. 8 for atom label definitions.
[c]Reference 16.
[d]Reference 15.
[e]Fixed.
[f]Reference 15, AIP-document No. PAPS JCPSA 81-2339-8 (all frequencies in column).
[g]Current work (all frequencies in column).

dispersed fluorescence.[15] The systematic lowering of frequencies and improved geometry is evidence that QCISD more accurately describes the electronic structure of CH_2CHO $\tilde{X}(^2A'')$. Presumably, basis set extension for QCISD would further improve the comparison of theory to experiment. The comparison between QCISD and CASSCF for the ground state suggests that the CASSCF frequencies for the $\tilde{B}$ state are also too high. This will be useful in interpreting the photofragment yield spectrum in Sec. IV A.

IV. ANALYSIS

In this section we analyze the vibrational structure in the CH_2CHO photofragment yield spectrum and present Monte Carlo simulations of noncoincident photofragment TOF distributions.

A. Photofragment yield spectrum

The vinoxy radical has 12 vibrational modes which have been assigned principal characters by Yamaguchi[23] as given in Table V: 3 out-of-plane a'' modes, 6 in-plane a' modes involving the heavy atoms, and 3 high frequency a' modes which are primarily hydrogen stretches. The large number of totally symmetric modes makes the assignment of the vibrational structure in the PFY spectrum nontrivial. We follow a systematic procedure, simulating the spectrum with the aid of *ab initio* frequencies. Starting with the lowest peaks in the spectrum of Fig. 2(b), the fundamental vibrations are assigned to a mode, the spectrum is simulated using approximate Franck–Condon factors (FCF) from Yamaguchi,[23] the vibrational constants are refined, and certain peaks at higher energy in the experimental spectrum are assigned as combination bands. Higher frequency vibrational modes are then added, one by one, and the process is repeated until the majority of the peaks in the spectrum are predicted by the simulation.

The simulated CH_2CHO spectrum is shown in Fig. 2(a), the peak assignments are listed in Table I, and the frequencies for the $\tilde{B}$ state obtained from our analysis are listed in Table V. Since the intensities in the simulation mimic the FCFs for absorption, the predicted intensity for several of the lowest energy transitions is too great. The photodissociation yield Φ_{diss} for these transitions is small, so they are not as intense in the PFY spectrum as in the absorption and LIF spectra. In the region where no fluorescence is observed, the absorption and photofragment yield intensities should be identical, since essentially all the excited molecules dissociate rather than fluoresce.

Using this iterative method we assign progressions in all six of the heavy atom a' modes, ν_4–ν_9, and 2 of the a'' modes, ν_{10} and ν_{11}. The vinoxy radical is planar in both the $\tilde{X}$ and $\tilde{B}$ states,[15] so that (in the absence of vibronic coupling), excitations in nontotally symmetric a'' vibrations are allowed only for $\Delta\nu=0,\pm2,\pm4,\ldots$. Due to the large change in *ab initio* frequencies of the a'' modes between the $\tilde{X}$ and $\tilde{B}$

states, it is not surprising that these modes are active. Our vibrational assignments agree with those of Gejo *et al.*[17] except for their assignment of ν_6=1406 cm^{-1} and ν_5=1433 cm^{-1}, which contrast with our assignments of ν_6=1274 cm^{-1} and ν_5=1406 cm^{-1}. Our assignment of the ν_6 frequency seems to be more in line with the CASSCF *ab initio* frequencies (Table V) which are consistently 7%–11% higher than experiment for the $\tilde{X}$ state. Overall we find a more consistent match of the simulated and experimental PFY spectrum with our assignments. Note that not all of the experimental peaks listed in Table I are assigned, and that the assignment of the peak at 29 976 cm^{-1} to the $8_0^1 11_0^1$ transition requires vibronic coupling that presumably involves the $\tilde{A}(^2A')$ state.

A comparison of the photofragment yield spectrum of CH_2CHO in Fig. 2(b) with the simulation in Fig. 2(a) and the LIF spectrum[15] shows mode specific competition between fluorescence and dissociation for the lower vibrational levels of the $\tilde{B}$ state, with excitation of a'' vibrational modes resulting in higher Φ_{diss} than nearby levels in which only a' modes are excited. For example, excitation of the 11_0^2 and 10_0^2 transitions (a'') at excess energies of 547.7 and 873.5 cm^{-1}, respectively, results in a significantly higher Φ_{diss} than the nearly isoenergetic 9_0^1 and 8_0^1 transitions (a') at 449.0 and 917.6 cm^{-1}. The implications of this effect will be discussed further in Sec. V E.

The photofragment yield spectrum of CD_2CDO in Fig. 2(c) appears substantially different than that of CH_2CHO. The differences between these spectra arise for two reasons. First, the vibrational levels in the $\tilde{B}$ state are shifted to lower frequency upon deuteration; their *ab initio* values have been calculated by Yamaguchi.[23] Therefore, deuteration will change both the positions and the FCFs of the $\tilde{B}(^2A'')\leftarrow\tilde{X}(^2A'')$ absorption spectrum in CD_2CDO. Second, the quantum yield for dissociation as a function of photon energy is different than that of CH_2CHO. In particular, we cannot detect any resolved dissociation signal for photon energies less than 29 828 cm^{-1}, implying that the dissociation rate at low excess energies is slower than that for CH_2CHO. However, the intense cluster of six peaks around 29 975 cm^{-1} implies a substantial increase in the dissociation rate $\approx$1100 cm^{-1} above the origin level. This energy is similar in magnitude to the energy at which fluorescence is quenched and the photofragment angular distributions become anisotropic in CH_2CHO. Due to the lack of structure in the first 1000 cm^{-1} of the PFY spectrum of CD_2CDO, we have not attempted to assign the vibrational modes in this spectrum. The data from a full LIF spectrum of the deuterated species would make assignments more tractable.

B. Monte Carlo forward convolution for CD_2CDO TOF distributions

The noncoincidence TOF distributions in Fig. 6 are due to *all* the fragments produced in the dissociation of the vinoxy radical. A direct inversion of this data to give the translational energy and angular distributions for all product channels is clearly not feasible. However, because the energy and angular distributions of Channel 1 (CD_3+CO) have already been determined, any new features in the observed noncoincidence TOF distributions must be due to a second product channel. We can extract information on the dynamics of this channel by employing a forward convolution technique to simulate the experimental TOF data. In this analysis, a set of product channels, each with its own $P(E_T)$ distribution and anisotropy parameter β, serves as inputs to a Monte Carlo forward convolution program[29] which generates the 1-D TOF distributions that would be observed in our experiment based on the apparatus geometry and finite spatial acceptance of the detector. By comparing the predicted TOF distributions with the experimental distributions, the initial estimate for channels other than CD_3+CO can be refined as needed until the simulated and observed TOF distributions agree.

For Channel 1, the $P(E_T)$ distributions in Fig. 5 are used, and β=0.4 is taken as the energy-independent value of the anisotropy parameter; this is the average value of β at the excitation energies where TOF measurements were taken. The contribution of CD_3 and CO to the total TOF is shown in Fig. 7(a). The remaining features in the TOF data are the narrow spike in the middle of the distribution and the broad wings at the edges of the spectrum. Only Channels 2 and 3, CD_2CO+D and DCCO+D_2, are consistent with these features. The thermodynamics for the two channels differ by only 0.06 eV,[11,26,27] making them both energetically feasible. However, the kinematics are quite different; if D_2+DCCO is assumed to be the sole heavy–light channel, the $P(E_T)$ distributions required to simulate the broad wings extend beyond the maximum E_T allowed by thermodynamics. Moreover, the D+CD_2CO channel results from simple bond fission and should have at most a small exit barrier ($<$0.3 eV), while elimination of D_2 would pass through a more strained four-center transition state, causing a substantial barrier on the potential energy surface. Therefore, elimination of D_2 should be kinetically disfavored compared to simple bond fission, and we propose that Channel 2 is the only channel other than Channel 1 contributing to the TOF distributions.

Because we expect a rather small exit barrier for Channel 2, a plausible initial estimate for the $P(E_T)$ distribution is a prior distribution,[51] i.e., the approximate distribution expected for statistical dissociation with no barrier, shown in Fig. 7(c) (dashed line). However, the experiment is most sensitive to translational energies $E_T>0.5$ eV, and agreement with the data is much better with a slower fall-off at higher E_T shown by the solid line in this figure. We find that β=0.25 gives the best overall fit using this $P(E_T)$ distribution; larger values of β cannot fit data from both polarizations simultaneously. An additional parameter in the simulations is the detection efficiency of D atoms. This should be independent of the photon energy or polarization, and only values in the range of $\approx$8% efficiency can simultaneously reproduce the data at all four photon energies and both laser polarizations.

The resulting overall fits including the contributions for Channels 1 and 2 are shown as solid lines in Figs. 6 and 7(a) and are in good agreement with the data. The $P(E_T)$ distri-

butions for Channel 2 at all measured photon energies are similar to the distribution in Fig. 7(c), peaking close to zero and with a maximum E_T of around 1.3 eV. This approximate independence from the photon energy was also seen in Channel 1.

The branching ratio of Channels 2 to 1 derived from the simulation of the TOF distributions is 4:1, with negligible dependence on the photon energy. However, because of the insensitivity of the simulation to low translational energies for Channel 2, we estimate that the true branching ratio could range from 2:1 to 6:1. In any event, we believe that CD_2CO+D is the major product channel at all photon energies studied.

V. DISCUSSION

A. Implications of the experimental data

The most important experimental results are as follows. (1) The photofragment yield spectrum shows that CH_2CHO predissociates across the entire $\tilde{B}(^2A'')\leftarrow\tilde{X}(^2A'')$ band. Predissociation and fluorescence are competing processes, with predissociation dominating at energies >1400 cm^{-1} above the $\tilde{B}$ state origin. (2) Below 1400 cm^{-1}, there is some mode specificity in the competition between fluorescence and dissociation, with vibrational levels in which a'' modes are excited dissociating more rapidly than nearby a' levels. (3) The CH_3+CO photofragment angular distribution is isotropic at low energies but becomes anisotropic with $\beta(E_T)>0$ above 1400 cm^{-1}. (4) The photofragment translational energy distributions $P(E_T)$ are relatively independent of excitation energy for Channels 1 and 2, and peak at energies well below the maximum allowed by energy conservation.

The last observation is the most important as it implies that dissociation does not occur by coupling of the $\tilde{B}$ state to a repulsive surface correlating directly to products. Dynamics occurring on a repulsive excited state typically deposit a large fraction of the available energy into relative translation of the fragments, and one expects the $P(E_T)$ distributions to shift towards higher E_T as the excitation energy is increased; both of these effects were observed in photodissociation of CH_3O,[10] for example. The $P(E_T)$ distributions for CH_2CHO imply a different mechanism, in which Channel 1 (CH_3+CO) results from the dissociation of a strongly bound state over a substantial barrier, whereas Channel 2 ($H+CH_2CO$), for which the $P(E_T)$ distributions peak near $E_T=0$, results from dissociation of such a state over a much smaller barrier.

In the following discussion, this mechanism is considered in more detail. We will show that the set of results obtained here is consistent with the initial electronic excitation being followed by internal conversion (IC). This process eventually populates the ground electronic state where energy randomization occurs, followed by decomposition to the two observed product channels. We first consider the asymptotic final state distributions for the two channels and the branching ratios that would be expected from such a mechanism; most of this discussion focuses on Channel 1, since considerably more detailed data are available than for Channel 2. We then consider how IC might connect the initially excited electronic state to the ground state on which dissociation occurs.

B. Dissociation mechanism and product state distributions: CH_3+CO

1. Barrier to dissociation of Channel 1

The $P(E_T)$ distributions for Channel 1 all peak in the range of $E_T=0.9-1.0$ eV. If this channel resulted from statistical dissociation on a surface with no exit barrier (i.e., no barrier with respect to products), one would expect a translational energy distribution described by phase space theory or a prior distribution, peaking very near $E_T=0$. This clearly disagrees with our experimental evidence. On the other hand, the distributions for Channel 1 are consistent with statistical dissociation over an exit channel barrier. Such a process is statistical in the sense that energy randomization occurs prior to dissociation, but passage over the barrier results in rapid release of energy which is *not* statistically distributed among the product degrees of freedom. Instead, a substantial fraction of the barrier height is converted to fragment translation, resulting in a $P(E_T)$ distribution peaking at 40%–80% of the barrier height.[52] Therefore, our experimental $P(E_T)$ distributions for Channel 1 imply a barrier with respect to products of between 1.1 and 2.2 eV in the CH_3+CO exit channel. The nature of this barrier can be inferred from our *ab initio* calculations. Figure 8 shows that the reaction coordinate to Channel 1 on the ground state surface involves passage over two barriers: TS1, the barrier to isomerization (via a 1,2 hydrogen shift) between CH_2CHO and the acetyl radical, CH_3CO, and TS3, the barrier to elimination of CO from CH_3CO. TS1 is the higher energy transition state and is found to be a nearly planar CH_2CO moiety with the out-of-plane migrating H atom shared between the two carbon atoms. This isomerization is reasonably facile because the a'' unpaired electron on the methylene carbon in the $\tilde{X}$ state is available for bonding with the migrating H atom.

The calculated energies of TS1 and TS3 are 1.74 and 0.40 eV, respectively, above the CH_3+CO products. The latter value agrees with the experimentally determined exit barrier to CH_3CO dissociation, 0.36 eV,[44,45] but is too low to account for our $P(E_T)$ distributions for CH_2CHO dissociation. On the other hand, the calculated barrier height for TS1 is in the range expected based on the $P(E_T)$ distributions. The simplest mechanism consistent with our data and the PES is that after traversing TS1, dissociation occurs so rapidly that the small barrier TS3 does not trap the radicals in the CH_3CO well, nor does TS3 control the final product states. Therefore, we can envision, for the purpose of understanding the product state distributions, a simplified PES with only a single barrier (TS1) between CH_2CHO $\tilde{X}(^2A'')$ and CH_3+CO. This hypothesis can be tested by comparing the $P(E_T)$ distributions we observe (Fig. 4) against the predictions of photodissociation dynamics models (see Sec. V B 2).

As an aside, we note that if CH_2CHO $\tilde{A}(^2A')$ were formed by IC, the 1,2 hydrogen shift would be much less

favorable because the there is a C═C double bond in this state.[21,24] Forming the transition state analogous to TS1 therefore requires significant torsional distortion of the C═C double bond to a nonplanar geometry, in addition to the strain energy associated with the tight transition state, resulting in a high energy transition state. It therefore unlikely that CH_3+CO production is feasible on the $\tilde{A}$ surface.

2. Statistical adiabatic impulsive model

In this section, we present a simple model to describe the dissociation dynamics of a molecule undergoing statistical decomposition over a barrier. Simple models predicting the $P(E_T)$ distribution for molecular photodissociation can be divided into two categories. *Statistical models* predict the $P(E_T)$ distribution for unimolecular dissociations through a loose transition state (TS). Examples include prior distributions,[51] phase space theory,[53] separate statistical ensembles method,[54] and the statistical adiabatic channel model.[55] *Sudden approximation models*, such as Franck–Condon (FC) mapping[56] and the impulsive model,[57] are more suitable for predicting the $P(E_T)$ distribution for direct dissociation on a repulsive potential or over a barrier associated with a tight TS.

For excitation energies in proximity to the barrier height, the repulsive nature of the potential dominates the dissociation process, and the sudden approximation can often predict the product state distributions. However, for excitation energy in significant excess of the barrier height, which we believe is the case for Channel 1, a more general approach is required combining both statistical and sudden models. As an example of such an approach, North *et al.*[58] have developed the barrier impulsive model which predicts the *average* energy in product translation, rotation, and vibration for dissociation over a potential barrier. We have developed a qualitatively similar approach, the statistical adiabatic impulsive (SAI) model, in order to predict the $P(E_T)$ *distributions* for Channel 1. The SAI model is described briefly here and will be presented in more detail elsewhere.[59]

As shown in Fig. 9(a), the total energy available to the products ($E_{\text{avail}}=h\nu-D_0$) is divided into two separate energy reservoirs: a statistical reservoir (the energy from the TS up to the total available energy, i.e., $E_{\text{stat}}=E_{\text{avail}}-E_{\text{TS}}$) and an impulsive reservoir (the energy of the TS relative to the ground state energy of the products, i.e., $E_{\text{imp}}=E_{\text{TS}}$). The energy of the TS, E_{TS}, corresponds to the zero-point level of TS1 with respect to the CH_3+CO products. The SAI model requires knowledge of the TS geometry, frequencies, and normal modes, which in the present case are taken from our *ab initio* calculations.

We assume that energy is randomized among all vibrational modes at the transition state (i.e., the top of the barrier). For the statistical reservoir, each vibrational mode at the transition state is correlated[58] with a particular *product* vibrational (V), rotational (R), or translational (T) degree of freedom. For example, in the CH_2CHO system at TS1, two skeletal bending modes correlate with product R, and two stretching modes and the reaction coordinate correlate with product T. The remaining seven vibrational modes at the TS are the only modes that asymptotically correlate with product V. These designations are given next to vibrational frequencies for TS1 in Table IV. Next we make the assumption that beyond the TS the internal motions evolve adiabatically to products. This assumption seems justified because the fragments will separate rapidly after traversing the transition state region. Hence, for each possible vibrational state at the TS, the quantum numbers in each mode are preserved throughout the dissociation. The vibrational energy deficit or surplus for each state is assumed to flow freely between V

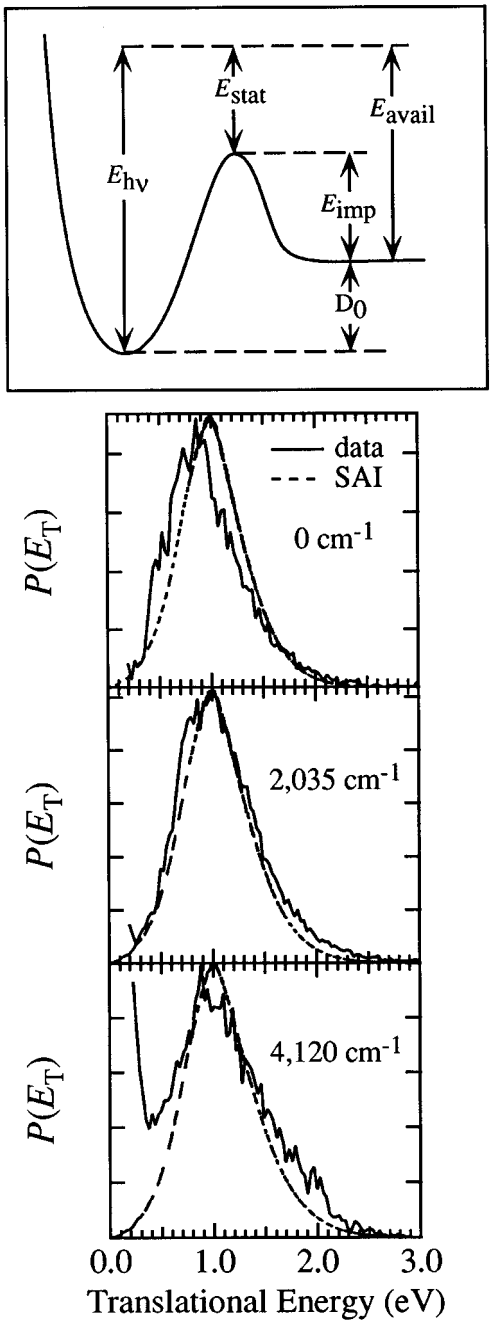

FIG. 9. (a) Definition of terms in the statistical adiabatic impulsive (SAI) model. (b) Comparison of SAI (---) and experimental (—) $P(E_T)$ distributions for CH_3+CO at three selected energies.

and T degrees of freedom, while energy at the TS in the two skeletal bends goes entirely into product R. This yields the internal energy $P_{\rm stat}(E'_{\rm int})$ distribution for the statistical reservoir. The product state distribution of the fragments from this reservoir is not strictly statistical in the sense of a prior or PST distribution, in which the energy is randomized among fragment states. Rather, energy is statistically distributed at the tight TS and evolves adiabatically to the products.

The impulsive reservoir's contribution to the product energy distributions is determined by the TS geometry. For this reservoir, the vibrational energy distribution of the products is determined by Franck–Condon projection of the zero-point TS wave function on to the asymptotic product wave functions. For each final vibrational state, the remaining energy in the impulsive reservoir is partitioned between translation and rotation using a rigid impulsive model based on the TS geometry. The $P_{\rm imp}(E''_{\rm int})$ distribution for the impulsive reservoir is the sum of the impulsive model result for each combination of vibrational product states, weighted by their FC projection factors. For vinoxy dissociation through TS1, approximately 55% of the exit barrier height evolves into E_T. The $P_{\rm imp}(E''_{\rm int})$ distribution is independent of excitation energy, as the energy of this reservoir remains constant. This provides an explanation for the maximum intensity at $\approx$0.9 eV in the experimental $P(E_T)$ distributions and its relative independence on excitation energy.

Finally, the overall $P(E_{\rm int})$ distribution is created by a convoluting the statistical and impulsive distributions

$$P(E_{\rm int}) = \int_0^{E_{\rm stat}} P_{\rm stat}(E'_{\rm int}) \cdot P_{\rm imp}(E_{\rm int} - E'_{\rm int}) dE'_{\rm int}. \qquad (11)$$

The translational energy distribution $P(E_T)$ is then obtained by plotting $P(E_{\rm int})$ vs $E_T = E_{\rm avail} - E_{\rm int}$. We emphasize that the SAI model contains no adjustable parameters and conserves energy in each separate reservoir and therefore for the overall process.

The predictions of the SAI model and experimental $P(E_T)$ distributions are shown in Fig. 9(b) for three excitation energies. The reasonable agreement between the model and the data lends credence to the idea that the $P(E_T)$ distributions for Channel 1 are determined largely by the height and geometry of the vinoxy/acetyl isomerization barrier.

3. Comparison with CH_3CO decomposition

In experiments related to the vinoxy system, several groups have examined the fragmentation of the acetyl radical, $CH_3CO \rightarrow CH_3 + CO$. In these experiments, CH_3CO is not laser-excited to a state of specific energy, as in the present work on CH_2CHO, but is instead prepared with a distribution of internal energies by either (i) photodissociation of acetyl halides CH_3COX (X=Cl,[45,60] Br,[60] I[61]) and acetone,[58] or (ii) charge neutralization of the acetyl cation, CH_3CO^+.[62,63] In the photodissociation experiments, CH_3CO is formed with average internal energy $\langle E_{\rm int}\rangle$=0.8, 1.3, 1.5, or 1.7 eV, depending on the photon energy and the identity of the primary photofragment (Cl, Br, I, or CH_3). In *all* cases the $P(E_T)$ distributions for CH_3+CO peak at 0.22–0.3 eV. These experiments offer convincing evidence that the translational energy distributions are determined by the 0.36 eV exit barrier (TS3) and depend only weakly on $\langle E_{\rm int}\rangle$. In addition, the significant differences in the $P(E_T)$ distributions in these experiments compared to ours supports our hypothesis that the dissociation dynamics of $CH_2CHO \rightarrow CH_3+CO$ are not determined by TS3, but rather by TS1.

In the second set of experiments, Körnig *et al.*[62] and Hop and Holmes[63] have studied the dissociation of CH_3CO produced by charge neutralization of CH_3CO^+ with Na, K, or Cs atoms. The work by Körnig *et al.* is particularly relevant to our results, as they measured the translational energy release of the dissociation to CH_3+CO in a fast beam dissociation experiment similar to ours. They estimate that excited acetyl is created with $\langle E_{\rm int}\rangle \approx 1.9$, 2.7, or 3.1 eV of internal energy, when formed by the three alkali atoms, respectively. Their $P(E_T)$ distributions depend little on the alkali atom used, and are remarkably similar to our distributions in Fig. 4, peaking at 0.8 eV. However, since CH_3CO^+ has a linear[64] CCO backbone, whereas neutral CH_3CO $\tilde{X}(^2A')$ has $\angle$(CCO)=127°, the Franck–Condon overlap of the ion with the acetyl ground state is expected to be poor. Nimlos *et al.*[39] predict that an excited state of acetyl, the linear CH_3CO $\tilde{A}(^2A'')$ state, lies $\approx$1.3 eV above the ground state. We therefore surmise that in charge neutralization experiments, CH_3CO is formed in the excited $\tilde{A}$ state, due to better FC overlap with the linear cation. Furthermore, the $P(E_T)$ distributions of Körnig are not consistent with the work described above by North[45,58,60] and Kroger,[61] in which dissociation definitely occurs on the ground state PES. Therefore, we can only conclude that the dissociation to CH_3+CO studied by Körnig either occurs on an excited state surface, or that they grossly underestimate the value of $\langle E_{\rm int}\rangle$ of the acetyl radicals. In either case, the resemblance of their $P(E_T)$ distributions to ours seems to be purely coincidental.

C. Dissociation mechanism and product state distributions: $H+CH_2CO$

The $P(E_T)$ distributions for Channel 2 peak near $E_T=0$. Using the same arguments as in Sec. V B 1, this channel likely results from statistical dissociation over at most a small exit barrier along the reaction coordinate. From Fig. 8, we can determine if such a mechanism is plausible. There are three possible routes to $H+CH_2CO$. The first two possibilities are direct C–H bond fission from CH_2CHO $\tilde{X}(^2A'')$ or CH_2CHO $\tilde{A}(^2A')$ as shown on the left side of Fig. 8. The third route is direct C–H bond fission from the isomerization product CH_3CO, shown on the right side of Fig. 8.

All three routes have barriers with respect to products, because the reverse reaction of H $(^2S)+CH_2CO$ $\tilde{X}(^1A_1)$ involves a radical reacting with a closed-shell molecule. TS2, the barrier to C–H bond fission from CH_3CO, lies only 0.24 eV above the product asymptote. However, TS2 lies 2.05 eV above the CH_3CO minimum, whereas the barrier to C–C bond fission, TS3, lies only 0.75 eV above CH_3CO. Once isomerization to CH_3CO occurs, Channel 1 should therefore be strongly favored over Channel 2. However, we observe

TABLE VI. RRKM dissociation rate constants.

Photon energy	$k_1(E)$ ($s^{-1}/10^{11}$)	$k_2(E)$ ($s^{-1}/10^{11}$)
$h\nu=28\,785$	1.0	4.2
$h\nu=31\,000$	1.6	6.5
$h\nu=33\,300$	2.4	9.3

that the Channel 2: Channel 1 branching ratio is approximately 4:1. It is therefore unlikely that passage over TS2 contributes significantly to Channel 2.

CH_2CHO $\tilde{X}(^2A'')$ correlates adiabatically (in C_s symmetry) with the $\tilde{a}(^3A'')$ excited state of ketene, while the first excited vinoxy state, CH_2CHO $\tilde{A}(^2A')$, correlates adiabatically (over barrier TS4) with ground state ketene $\tilde{X}(^1A_1)$. At nonplanar geometries the two surfaces may couple through an avoided crossing, allowing the dissociation pathway CH_2CHO $\tilde{X}(^2A'')\rightarrow CH_2CO$ $\tilde{X}(^1A_1)+H$. The exit barrier TS5 along this path is suggested in Fig. 8, although we have not definitively located a nonplanar transition state in our calculations. We adopt an exit barrier height of 0.13 eV[65] advocated by Benson for the addition reaction $H+CH_2CO$ on the ground state surface. The transition state frequencies for TS5 (Table IV) are also estimated using values given by Benson.[66] TS5 lies considerably lower in energy than TS4 with respect to the $H+CH_2CO$ products, and the $P(E_T)$ distributions for Channel 2 are more consistent with dissociation on the ground state surface over TS5.

D. Product branching ratio

In this section we consider the relationship between the product branching ratio and the proposed mechanism for Channels 1 and 2. TS5, the barrier along the most likely reaction path for Channel 2, lies slightly lower in energy (1.63 eV) with respect to the CH_2CHO $\tilde{X}(^2A'')$ minimum than TS1, the isomerization barrier (1.78 eV). In addition, TS5 is a ''looser'' transition state than TS1, since it involves bond fission rather than rearrangement. One would therefore expect statistical dissociation on the ground state to favor Channel 2, in agreement with the experimental results that show this channel to be favored by about 4:1.

To put this argument on a more quantitative footing, we can compute the RRKM rate constants $k=[W(E^+)]/[h\rho(E)]$ for the two elementary reaction steps

$$CH_2CHO \xrightarrow{k_1} CH_3CO, \tag{12}$$

$$CH_2CHO\ \ \tilde{X}(^2A') \xrightarrow{k_2} H+CH_2CO\ \ \tilde{X}(^1A_1), \tag{13}$$

where $W(E^+)$ is the total number of available vibrational states at the transition state, h is Planck's constant, and $\rho(E)$ is the density of reactant vibrational states. Both $\rho(E)$ and $W(E^+)$ are calculated using the Beyer–Swinehart algorithm and the vibrational frequencies for the reactant and transition states from Table IV. The resulting rate constants at a few representative photon energies are given in Table VI. The dissociative lifetimes on the ground electronic surface are in the range of 1–10 ps.

Based on the discussion in Sec. V B, isomerization should be the rate-limiting step for Channel 1, so the branching ratio can be computed from these two elementary reactions alone. The ratio k_2/k_1 is $\approx$4:1, a value which matches the experimental branching ratio. Although this excellent agreement may be fortuitous, it further supports our proposed mechanism in which Channels 1 and 2 result from dissociation of CH_2CHO on its ground state potential energy surface, with the dynamics and branching ratio largely determined by the transition states TS1 and TS5, for isomerization and C–H bond fission, respectively.

E. Internal conversion

The preceding discussion strongly indicates that Channels 1 and 2 result from dissociation on the ground state potential energy surface, but has not considered how electronic excitation of the $\tilde{B}$ state is converted to vibrational excitation of the $\tilde{X}$ state. There are two likely pathways for this internal conversion process. The simplest is direct internal conversion from the $\tilde{B}(^2A'')$ to $\tilde{X}(^2A'')$ states, with the radiationless transition rate determined by Fermi's golden rule. On the other hand, the vinoxy radical has two low-lying excited states in addition to the $\tilde{B}(^2A'')$ state, namely the $\tilde{A}(^2A')$ and $\tilde{C}(^2A')$ states, with term values of 0.99 eV (experimental[13]) and 4.60 eV (predicted[24]), respectively, at planar geometries. One must therefore consider whether energy flows to the $\tilde{X}(^2A'')$ state via one or both of these states.

Experimental data on the fluorescence and dissociation rates are relevant to the nonradiative relaxation mechanism. Barnhard *et al.*[18] and Rohlfing[67] have measured fluorescence lifetimes on the order of 100 ns for several vibrational levels of the $\tilde{B}$ state with less than 1400 cm^{-1} excess energy. These values are entirely consistent with the photofragment angular distributions for Channel 1 in this energy range, all of which are isotropic, indicating that the excited radical lives for many rotational periods before dissociation occurs. The nonradiative rates in this energy range must be comparable to the fluorescence rates since fluorescence and dissociation are competitive. Given that the RRKM rate constants (Table VI) are at least $10^{11}s^{-1}$, it is clear that nonradiative relaxation is the rate-limiting step for dissociation below 1400 cm^{-1}.

However, above 1400 cm^{-1}, the fluorescence yield drops abruptly[14,15] and the photofragment angular distributions become anisotropic. This indicates a rapid increase in the nonradiative rate. We can quantify this increase by recognizing that the anisotropic angular distributions above 1400 cm^{-1} imply a lifetime of the excited radical with respect to dissociation of less than a rotational period. The appropriate rotational constant for calculating the rotational period of this nearly prolate symmetric top is $(B+C)/2=0.35$ cm^{-1}; using $J=10$ $(K=0)$ as an average value, the rotational period about the b and c axes is approximately 5 ps. In order for dissociation to occur on this time scale, the overall internal conversion process populating the ground state must be at least this fast, so its rate must increase by about 4 orders of magnitude in a relatively narrow interval around 1400 cm^{-1} excess energy.

Based on Fermi's golden rule, one would expect the internal conversion rate from the initially excited levels of the $\tilde{B}(^2A'')$ state to highly excited levels of the $\tilde{X}(^2A'')$ state to increase with excess energy in the $\tilde{B}$ state.[68] However, it is unlikely that this effect alone could produce the abrupt increase in the internal conversion rate implied by the experiments. The abrupt drop in fluorescence quantum yield is similar to benzene, where the fluorescence quantum yield of the S_1 ($^1B_{2u}$) state drops considerably at excess energies above 3000 cm^{-1}.[69] The mechanism of the nonradiative process responsible for this effect, known as ''channel three,'' is still under discussion, but there appears to be a consensus that it is due to a combination of intramolecular vibrational redistribution (IVR) to dark levels of the S_1 state followed by $S_1 \rightarrow S_0$ internal conversion, with the onset of fast IVR coinciding with the drop in fluorescence quantum yield.[70–72] While such a mechanism might explain the fluorescence cutoff in vinoxy, it does not explain the enhanced dissociation rate, because there is no reason to believe that the relaxed levels of the $\tilde{B}$ state populated by IVR should be so much more strongly coupled to the $\tilde{X}$ state than the originally populated state.

An alternative explanation for the abrupt fluorescence cutoff and increased dissociation rate is the possibility of a curve crossing between the $\tilde{B}$ state and another low-lying state at an excess energy in the range of 1400 cm^{-1}. The calculations by Yamaguchi[24] predict that the energy of the $\tilde{A}$ state rises by about 2.2 eV if the vinoxy radical is twisted by 90° about the C–C bond due to the double-bonded character of the C–C bond in the $\tilde{A}$ state, whereas the energies of the $\tilde{B}$ and $\tilde{A}$ states are relatively insensitive to torsional distortion. The net result is that the $\tilde{B}$ and $\tilde{A}$ states become nearly degenerate at a dihedral angle of 90°, suggesting that a low energy crossing may occur. This calculation also predicts that the $\tilde{C}(^2A')$ state, which lies 1.1 eV above the $\tilde{B}$ state in the planar geometry, drops in energy as the radical as twisted and becomes nearly degenerate with the $\tilde{B}$ state. Thus low energy curve crossings with either the $\tilde{A}$ or $\tilde{C}$ states appear to be feasible.

The possible role of the $\tilde{A}$ or $\tilde{C}$ states is indirectly supported by the mode-specific effects seen below 1400 cm^{-1} where fluorescence and dissociation compete. As pointed out in Sec. IV A, excitation of a'' vibrational modes in the $\tilde{B}$ state enhances the dissociation yield compared to nearby levels in which only a' modes are excited. This observation is consistent with a radiationless transition through vibronic coupling between the $\tilde{B}(^2A'')$ state and an electronic state of A' symmetry,[68,73] with the $\tilde{A}(^2A')$ or $\tilde{C}(^2A')$ states as the most likely candidates.

The above arguments support the idea that nonradiative relaxation process above 1400 cm^{-1} involves coupling between the $\tilde{B}$ state and either the $\tilde{A}$ or $\tilde{C}$ states, rather than direct coupling with the $\tilde{X}$ state. However, dissociation does appear to occur on the ground state surface, so energy flow from the $\tilde{A}$ or $\tilde{C}$ state to the $\tilde{X}$ state must quite rapid for this mechanism to be valid. The $\tilde{B} \rightarrow \tilde{A}$ radiationless transition will result in highly excited species with substantial energy in the torsional vibration, whereas the transition to the $\tilde{C}$ state will produce radicals with relatively little vibrational energy. The $\tilde{B} \rightarrow \tilde{A}$ state is therefore more favorable based on the higher density of vibrational levels in the $\tilde{A}$ state compared to the $\tilde{C}$ state. In addition, since internal conversion rates generally increase with vibrational excitation in the initial state,[73] it seems a transition to the $\tilde{A}$ state is more likely to result in subsequent rapid internal conversion to the $\tilde{X}$ state than a transition to the $\tilde{C}$ state. Thus the overall internal conversion scheme most consistent with the experimental results and *ab initio* calculations is a two-step mechanism, $\tilde{B}(^2A'') \rightarrow \tilde{A}(^2A') \rightarrow \tilde{X}(^2A'')$, with the first step being rate-limiting below 1400 cm^{-1} excess energy.

VI. CONCLUSIONS

The spectroscopy and dissociation dynamics of the vinoxy radical presented in this paper have been obtained under well-defined experimental conditions. Internally cold radicals are laser excited to exact total energies and the nascent photofragments are probed as a function of photon energy, product channel, translational energy, and angular distribution. In concert with *ab initio* electronic structure calculations presented in this paper, we have explored the critical configurations on the potential energy surfaces, and presented a simple dissociation mechanism which is consistent with all the experimental and theoretical results. After initial excitation via the $\tilde{B}(^2A'') \leftarrow \tilde{X}(^2A'')$ transition, all observed vibrational levels of CH_2CHO predissociate. We assign transitions in the photofragment yield spectrum to eight vibrational progressions, two involving nontotally symmetric vibrational modes. At lower photon energies, the rate of nonradiative decay is mode specific, depending strongly on the symmetry of the vibrational mode excited in the $\tilde{B}$ state. The photofragment energy and angular distributions indicate that dissociation occurs by internal conversions to the ground state potential energy surface upon which dissociation proceeds to $H+CH_2CO$ and CH_3+CO with a branching ratio of roughly 4:1. The dramatic increase in the dissociation rate above 1400 cm^{-1} suggests a curve crossing of the $\tilde{B}$ state with the $\tilde{A}$ or $\tilde{C}$ states, followed by rapid internal conversion to the ground potential energy surface.

For the CH_3+CO channel, we show that the translational energy distribution of the fragments is determined by the $CH_2CHO \rightarrow CH_3CO$ isomerization barrier on the ground state potential energy surface. For this system, in which both the exit barrier height and the excess energy at the transition state are substantial. We have therefore developed the statistical adiabatic impulsive model,[59] which successfully predicts the observed $P(E_T)$ distributions with no adjustable parameters. Our results for this channel are discussed in light of previous investigations of unimolecular decomposition of the acetyl radical.

The hydrogen atom loss channel is probed by the time-of-flight distributions arising from CD_2CDO photodissociation. Although our information on this product channel is more limited, we find the simplest explanation consistent with our results is direct dissociation from vinoxy over a small barrier. This barrier is formed by an avoided crossing

between the CH_2CHO $\tilde{X}(^2A'')$ state, which correlates for planar geometries with $H+CH_2CO$ $\tilde{a}(^3A'')$, and the CH_2CHO $\tilde{A}(^2A')$ state, which correlates with $H+CH_2CO$ $\tilde{X}(^1A_1)$.

Together with detailed previous results of traditional optical spectroscopy, the present work on photodissociation of vinoxy sheds new light on the electronic states and dynamics of this prototypical alkenoxy free radical.

ACKNOWLEDGMENTS

This research is supported by the Director, Office of Energy Research, Office of Basic Energy Sciences, Chemical Sciences Division, of the U. S. Department of Energy under Contract No. DE-AC03-76SF00098. D.H.M. is grateful for a NATO research fellowship administered by the Royal Society, England. D.L.O. acknowledges Professor Robert Continetti for advice on forward convolution simulations, and Professor Bradley Moore for discussions of internal conversion mechanisms. We thank Dr. Eric Rohlfing for sharing his results prior to publication.

[1] R. Schinke, *Photodissociation Dynamics* (Cambridge University Press, Cambridge, 1993).
[2] L. J. Butler and D. M. Neumark, J. Phys. Chem. **100**, 12801 (1996).
[3] R. J. Cvetanovic and D. L. Singleton, Rev. Chem. Int. **5**, 183 (1984).
[4] A. M. Schmoltner, P. M. Chu, R. J. Brudzynski, and Y. T. Lee, J. Chem. Phys. **91**, 6926 (1989).
[5] D. J. Donaldson, I. V. Okuda, and J. J. Sloan, Chem. Phys. **193**, 37 (1995).
[6] V. Schmidt, G. Y. Zhu, K. H. Becker, and E. H. Fink, Ber. Bunsenges. Phys. Chem. **89**, 321 (1985).
[7] K. Lorenz and R. Zellner, Ber. Bunsenges. Phys. Chem. **88**, 1228 (1984); T. J. Wallington, R. Liu, P. Dagaut, and M. J. Kurylo, Int. J. Chem. Kinet. **20**, 41 (1988).
[8] C. K. Westbrook and F. L. Dryer, *Eighteenth Symposium (International) on Combustion* (Combustion Institute, Pittsburgh, 1981), p. 749.
[9] K. Brezinsky, Prog. Energy Combust. Sci. **12**, 1 (1986).
[10] D. L. Osborn, D. J. Leahy, E. M. Ross, and D. M. Neumark, Chem. Phys. Lett. **235**, 484 (1995).
[11] D. H. Mordaunt, D. L. Osborn, H. Choi, R. T. Bise, and D. M. Neumark, J. Chem. Phys. **105**, 6078 (1996).
[12] D. A. Ramsay, J. Chem. Phys. **43**, S18 (1965).
[13] H. E. Hunziker, H. Kneppe, and H. R. Wendt, J. Photochem. **12**, 377 (1981).
[14] G. Inoue and H. Akimoto, J. Chem. Phys. **74**, 425 (1981).
[15] L. F. DiMauro, M. Heaven, and T. A. Miller, J. Chem. Phys. **81**, 2339 (1984).
[16] Y. Endo, S. Saito, and E. Hirota, J. Chem. Phys. **83**, 2026 (1985); Y. Endo and E. Hirota, J. Mol. Spectrosc. **127**, 535 (1988).
[17] T. Gejo, M. Takayanagi, T. Kono, and I. Hanazaki, Chem. Lett. **XX**, 2065 (1993).
[18] K. I. Barnhard, M. He, and B. R. Weiner, J. Phys. Chem. **100**, 2784 (1996).
[19] G. B. Ellison, P. C. Engelking, and W. C. Lineberger, J. Phys. Chem. **86**, 4873 (1982); R. D. Mead, K. R. Lykke, W. C. Lineberger, J. Marks, and J. I. Brauman, J. Chem. Phys. **81**, 4883 (1984).
[20] N. C. Baird, R. R. Gupta, and K. F. Taylor, J. Am. Chem. Soc. **101**, 4531 (1979).
[21] M. Dupuis, J. J. Wendoloski, and W. A. Lester, Jr., J. Chem. Phys. **76**, 488 (1982).
[22] E. S. Huyser, D. Feller, W. T. Borden, and E. R. Davidson, J. Am. Chem. Soc. **104**, 2956 (1982).
[23] M. Yamaguchi, T. Momose, and T. Shida, J. Chem. Phys. **93**, 4211 (1990).
[24] M. Yamaguchi, Chem. Phys. Lett. **221**, 531 (1994).
[25] M. E. Jacox, Chem. Phys. **69**, 407 (1982).
[26] M. W. Chase, Jr., C. A. Davies, J. R. Downey, Jr., D. J. Frurip, R. A. McDonald, and A. N. Syverud, JANAF Thermochemical Tables, 3rd ed., J. Chem. Phys. Ref. Data **14**, (1985), Suppl. No. 1.; S. G. Lias, J. E. Bartmess, J. F. Liebman, J. L. Holmes, R. D. Levin, and W. G. Mallard, Gas-Phase Ion and Neutral Thermochemistry, *ibid*. **17**, (1988), Suppl. No. 1.
[27] J. T. Niiranen, D. Gutman, and L. N. Krasnoperov, J. Phys. Chem. **96**, 5881 (1992); C. W. Bauschlicher, Jr., *ibid*. **98**, 2564 (1994).
[28] D. L. Osborn, H. Choi, and D. M. Neumark, Adv. Chem. Phys. (in press).
[29] R. E. Continetti, D. R. Cyr, D. L. Osborn, D. J. Leahy, and D. M. Neumark, J. Chem. Phys. **99**, 2616 (1993).
[30] R. E. Continetti, D. R. Cyr, R. B. Metz, and D. M. Neumark, Chem. Phys. Lett. **182**, 406, 1991.
[31] D. R. Cyr, R. E. Continetti, R. B. Metz, D. L. Osborn, and D. M. Neumark, J. Chem. Phys. **97**, 4937 (1992).
[32] D. L. Osborn, D. J. Leahy, D. R. Cyr, and D. M. Neumark, J. Chem. Phys. **104**, 5026 (1996).
[33] J. M. B. Bakker, J. Phys. E **6**, 785 (1973); **7**, 364 (1974).
[34] S. Gerstenkorn and P. Luc, *Atlas du Spectre d'Absorption de la Molecule d'Iode* (Centre National de la Recherche Scientifique, Paris, 1978).
[35] D. J. Leahy, D. L. Osborn, D. R. Cyr, and D. M. Neumark, J. Chem. Phys. **103**, 2495 (1995).
[36] D. P. de Bruijn and J. Los, Rev. Sci. Instrum. **53**, 1020 (1982).
[37] C. Martin, P. Jelinsky, M. Lampton, R. F. Malina, and H. O. Anger, Rev. Sci. Instrum. **52**, 1067 (1981).
[38] D. F. Ogletree, G. S. Blackman, R. Q. Hwang, U. Stark, G. A. Somorjai, and J. E. Katz, Rev. Sci. Instrum. **63**, 104 (1992).
[39] M. R. Nimlos, J. A. Soderquist, and G. B. Ellison, J. Am. Chem. Soc. **111**, 7675 (1989).
[40] R. N. Zare, Mol. Photochem. **4**, 1 (1972).
[41] GAUSSIAN 92, Revision C, M. J. Frisch, G. W. Trucks, M. Head-Gordon, P. M. W. Gill, M. W. Wong, J. B. Foresman, B. G. Johnson, H. B. Schlegel, M. A. Robb, E. S. Replogle, R. Gompets, J. L. Andres, K. Raghavachari, J. S. Binkley, C. Gonzalez, R. L. Martin, D. J. Fox, D. J. Defrees, J. Baker, J. J. P. Stewart, and J. A. Pople, Gaussian, Inc., Pittsburgh, 1992.
[42] GAUSSIAN 94, Revision C.3, M. J. Frisch, G. W. Trucks, H. B. Schlegel, P. M. W. Gill, B. G. Johnson, M. A. Robb, J. R. Cheeseman, T. Keith, G. A. Petersson, J. A. Montgomery, K. Raghavachari, M. A. Al-Laham, V. G. Zakrzewski, J. V. Ortiz, J. B. Foresman, J. Cioslowski, B. B. Stefanov, A. Nanayakkara, M. Challacombe, C. Y. Peng, P. Y. Ayala, W. Chen, M. W. Wong, J. L. Andres, E. S. Replogle, R. Gomperts, R. L. Martin, D. J. Fox, J. S. Binkley, D. J. Defrees, J. Baker, J. P. Stewart, M. Head-Gordon, C. Gonzalez, and J. A. Pople, Gaussian, Inc., Pittsburgh, 1995.
[43] S. Deshmukh, J. D. Myers, S. S. Xantheas, and W. P. Hess, J. Phys. Chem. **98**, 12535 (1994).
[44] K. W. Watkins and W. W. Word, Intern. J. Chem. Kinetics **7**, 855 (1974).
[45] S. W. North, D. A. Blank, and Y. T. Lee, Chem. Phys. Lett. **224**, 38 (1994).
[46] L. A. Curtiss, K. Raghavachari, G. W. Trucks, and J. A. Pople, J. Chem. Phys. **94**, 7221 (1991).
[47] J. L. Durant and C. M. Rohlfing, J. Chem. Phys. **98**, 8031 (1993).
[48] D. Hegarty and M. A. Robb, Mol. Phys. **38**, 1795 (1979); R. H. E. Eade and M. A. Robb, Chem. Phys. Lett. **83**, 362 (1981).
[49] J. J. McDouall, K. Peasley, and M. A. Robb, Chem. Phys. Lett. **148**, 183 (1988).
[50] J. A. Pople, M. Head-Gordon, and K. Raghavachari, J. Chem. Phys. **87**, 5968 (1987).
[51] R. D. Levine and J. L. Kinsey, in *Atom–Molecule Collision Theory—A Guide for the Experimentalist*, edited by R. B. Bernstein (Plenum, New York, 1979).
[52] A. M. Wodtke, E. J. Hintsa, and Y. T. Lee, J. Phys. Chem. **90**, 3549 (1986); X. Zhao, R. E. Continetti, A. Yokoyama, E. J. Hintsa, and Y. T. Lee, J. Chem. Phys. **91**, 4118 (1989).
[53] P. Pechukas and J. C. Light, J. Chem. Phys. **42**, 3281 (1965).
[54] C. Wittig, I. Nadler, H. Reisler, J. Catanzarite, and G. Radhakrishnan, J. Chem. Phys. **83**, 5581 (1985).
[55] M. Quack and J. Troe, Ber. Bunsenges. Phys. Chem. **79**, 469 (1975).
[56] M. D. Morse, K. F. Freed, and Y. B. Band, J. Chem. Phys. **70**, 3604 (1979).
[57] G. E. Busch and K. R. Wilson, J. Chem. Phys. **56**, 3626 (1972); A. F. Tuck, J. Chem. Soc., Faraday Trans. **73**, 689 (1977).
[58] S. W. North, D. A. Blank, J. D. Gezelter, C. A. Longfellow, and Y. T. Lee, J. Chem. Phys. **102**, 4447 (1995).
[59] D. H. Mordaunt, D. L. Osborn, and D. M. Neumark (in preparation).
[60] S. W. North, Ph.D. thesis, University of California, Berkeley, 1995.
[61] P. M. Kroger and S. J. Riley, J. Chem. Phys. **67**, 4483 (1977).

[62] S. Körnig, J. H. M. Beijersbergen, and J. Los, J. Phys. Chem. **94**, 611 (1990).
[63] C. E. C. A. Hop and J. L. Holmes, Int. J. of Mass Spectrom. Ion Proc. **104**, 213 (1991).
[64] R. H. Nobes, W. J. Bouma, and L. Radom, J. Am. Chem. Soc. **105**, 311 (1983).
[65] S. W. Benson, *Thermochemical Kinetics* (Wiley, New York, 1968), p. 140.
[66] Reference 65, pp. 205–207.
[67] E. A. Rohlfing (private communication).
[68] P. Avouris, W. M. Gelbart, and M. A. El-Sayed, Chem. Rev. **77**, 793 (1977).
[69] J. H. Callomon, J. E. Parkin, and R. Lopex-Delgado, Chem. Phys. Lett. **13**, 125 (1972).
[70] L. Wunsch, H. J. Neusser, and E. W. Schlag, Z. Naturforsch. Teil A **36**, 1340 (1981); U. Schubert, E. Riedle, H. J. Neusser, and E. W. Schlag, J. Chem. Phys. **84**, 6182 (1986).
[71] T. Suzuki and M. Ito, J. Chem. Phys. **91**, 4564 (1989).
[72] A. Helman and R. A. Marcus, J. Chem. Phys. **99**, 5011 (1993).
[73] E. S. Yeung and C. B. Moore, J. Chem. Phys. **60**, 2139 (1974).